Journal of Power Sources 195 (2010) 7609–7626

Contents lists available at ScienceDirect

Journal of Power Sources

journal homepage: www.elsevier.com/locate/jpowsour

Proton exchange membrane fuel cell multi-physical dynamics and stack spatial non-homogeneity analyses

F. Gao, B. Blunier*, A. Miraoui, A. El-Moudni

Université de Technologie de Belfort-Montbéliard, Rue Thierry Mieg, 90000 Belfort, France

ARTICLE INFO

Article history:
Received 21 January 2010
Received in revised form 27 April 2010
Accepted 2 June 2010
Available online 10 June 2010

Keywords:
PEM fuel cell
Stack
Dynamic phenomena
Non-homogeneity
Dynamic modelling

ABSTRACT

This paper presents a multi-physical dynamic fuel cell stack model. This model covers three major physical domains: electrical, fluidic and thermal. The dynamic model in each domain is presented. The fuel cell stack model is obtained by stacking method from a generalized single cell model, thus the spatial effect through the stack can be modelled and observed. The stack model is validated temporally and spatially against a Ballard NEXA 1.2 kW 47 cells fuel cell stack. Then, the dynamic behaviour in each physical domain is analysed. It can be approximated by a first order system, thus the expressions of time constants in different domain are obtained. Finally, the fuel cell stack spatial non-homogeneity is analysed. From the results, a fuel cell stack model reduction method is proposed in order to reduce the computation time during simulations. The reduced fuel cell stack model is validated against the full model.

1. Introduction

Fuel cells are one of the most promising candidates for the future clean and zero-emission transportation system. Among the different type of fuel cells, the proton exchange membrane fuel cell (PEMFC) is considered as the most adapted device for automotive applications, because of its low operating temperature, compactness and environmental friendly by-product [1]. Although the PEM fuel cell has a great advantage compared to conventional energy sources, its commercialization has not been achieved yet. Many researches have to be carried out and improvement are still needed such as performances, durability, and cost.

In mobile applications, one of the key features is the fuel cell dynamic behaviour. In this kind of application, the fuel cell is usually operated under transient state, because the power demand is not always constant. In addition, the fuel cell is a complex electrochemical system; its major physical domains cover electrical, fluidic and thermal. Thus, the dynamics in each domain should be analyzed in order to understand the dynamic behaviour of a fuel cell stack.

In the literature many investigations dealing with the fuel cell dynamic behaviour have been carried out. Krewer et al. [1] have investigated the dynamic behaviour of a DMFC (direct methanol fuel cell) by introducing a set of dynamic models but only the voltage overshoot dynamic has been discussed. Yan et al. [2] proposed a two-dimensional mass transport half cell model. Their results demonstrate that the mass transport dynamic at cathode side is less than 0.4 s in the fuel cell. Yan et al. [3] have investigated the fuel cell transients from the experimental tests using different methods. They found out that the temperature has a significant effect on the fuel cell performances. Iftikhar et al. [4] have proposed another fuel cell dynamic model which lay on the use of non-integer derivatives method. The highlight of their model is that it can predict dynamic responses on a wide frequency range. Lemes et al. [5] have developed a dynamic fuel cell system model including the fuel cell auxiliaries; however, only the cell voltage dynamic has been analysed. Zou et al. [6] have investigated the fluid pressure dynamic in the interdigitated flow field. The predicted results found that the response time is generally quite fast. Wu et al. [7] have proposed a two-dimensional, isothermal transient model to analyse the fuel cell dynamic under different humidification conditions. The thermal transients have not been considered in their work. Methekar et al. [8] have developed a linear controller for fuel cell with a model considering the thermal dynamics of the fuel cell. Meng [9] has introduced a transient two-phase non-isothermal fuel cell model in order to investigate the cell voltage and temperature dynamics. The conclusion has been made based on that the heat transfer process has the most significant effect on transient response, which affects the electrical and fluidic processes. Yalcinoz et al. [10] have proposed an analytical model for air-breathing PEM fuel cell, with temperature dynamics consideration. The temperature effect is considered as the most important effect in fuel cell

* Corresponding author. Tel.: +33 383583398; fax: +33 384583636
E-mail addresses: fei.gao@utbm.fr (F. Gao), benjamin.blunier@utbm.fr (B. Blunier), abdellatif.miraoui@utbm.fr (A. Miraoui), abdellah.el-moudni@utbm.fr (A. El-Moudni).

0378-7753/$ – see front matter © 2010 Elsevier B.V. All rights reserved.
doi:10.1016/j.jpowsour.2010.06.006

Nomenclature

Greek letters

α	symmetry factor in electrochemical reaction
ΔS	entropy change ($J\,mol^{-1}\,K^{-1}$)
$\delta_{(x)}$	layer thickness (m)
η_{act}	steady-state activation losses (V)
λ	thermal conductivity ($W\,m^{-1}\,K^{-1}$)
$\lambda(z)$	membrane water content
μ_{gas}	gas dynamic viscocity (Pa s)
$\rho_{(x)}$	density ($kg\,m^{-3}$)
ρ_{dry}	membrane dry density ($kg\,m^{-3}$)
τ	first order system time constant (s)

Roman letters

S	layer section area (m^2)
C_{dl}	double layer capacitance (F)
C_p	thermal capacity ($J\,kg^{-1}\,K^{-1}$)
D_{hydro}	hydraulic diameter (m)
D_{ij}	binary diffusion coefficient ($m^2\,s^{-1}$)
D_λ	membrane water diffusion coefficient ($m^2\,s^{-1}$)
E_{cell}	cell OCV voltage (V)
F	Faraday constant ($C\,mol^{-1}$)
$h_{(x)}$	heat transfert coefficient ($W\,m^{-2}\,K^{-1}$)
H_2O	water activity
i	stack current (A)
i_0	exchange current density ($A\,m^{-2}$)
$J_{(x)}$	liquid water mass flow rate ($kg\,s^{-1}$)
L	length (m)
$M_{(x)}$	molar mass ($kg\,mol^{-1}$)
M_n	membrane equivalent mass ($kg\,mol^{-1}$)
n	number of electron
$P_{(x)}$	pressure (Pa)
$Q_{(x)}$	heat flow rate ($J\,s^{-1}$)
$q_{(x)}$	mass flow rate ($kg\,s^{-1}$)
R	ideal gas constant ($J\,mol^{-1}\,K^{-1}$)
r	membrane local resistivity ($\Omega\,m$)
Re	Reynold number
R_{mem}	membrane electrical resistance (Ω)
s	Laplacien variable
$T_{(x)}$	temperature (K)
V	volume (m^3)
$V_{(x)}$	specific voltage (V)
V_s	fluid mean velocity ($m\,s^{-1}$)

Subscripts

A	anode
act	activation
amb	ambient
Back_diff	back diffusion
C	cathode
cell	single fuel cell
ch	channels
cond	conduction
contact	contact area
CV	control volume
drag	electro-osmotic drag
ext	external
fluid	fluid
forced_conv	forced convection
gas	gas
GDL	gas diffusion layer
H_2	hydrogen
H_2O	water
inlet	gas inlet
mass	convective mass flow
mem	membrane
nat_conv_radia	nature convection and radiation
O_2	oxygen
ohm	ohmic
outlet	gas outlet
sat	saturation
solid	solid
sources	thermal sources
tot	total

performance. Sun et al. [11] have done several experimental tests to explore the local current dynamics in the fuel cell. They found out that the local current dynamics can be very different even though the average current shows little dynamics. Other kinds of fuel cell dynamic experimental tests have been introduced by Lee et al. [12]; their results show that the stabilization time is affected by the cell temperature, the humidity and the voltage range.

The output voltage of a single cell is very low (about 0.4–1.0 V), that is why, in order to achieve a high power output (about some hundred watts in mobile devices and some kilowatts in automotive applications) [13], several cells have to be connected together to form a fuel cell stack. Each single cell in the stack has the same physical structure, but under working conditions, the cells states (temperature, voltage, pressures, etc.) can be different, because of different geometry positions or boundary conditions. These differences can lead to a non-homogeneous distribution of these values across the stack and decrease the fuel cell performances or even its life-time. Thus, for a high power fuel cell stack, this kind of non-homogeneity should also be considered.

Ju et al. [14] have developed a non-isothermal single fuel cell model to investigate the thermal non-homogeneity in one cell. But the fuel cell stack non-homogeneity has not been considered. Park and Li [15] have developed a non-isothermal fuel cell stack model. Different kinds of non-homogeneity in the stack have been discussed. Their results indicate that the effect of non-homogeneous temperature is predominant on the cell voltage variance between the cells voltages. Maharudrayya et al. [16] have presented the flow non-homogeneous distribution and pressure drop in multiple U-type and Z-type flow pattern, from a three-dimensional CFD simulation. The electrical and thermal domains have not been discussed. Khandelwal et al. [17] have introduced a transient one-dimensional fuel cell stack thermal model to investigate the heating strategies for cold-starts. From their results, the stack non-homogeneous temperature effect can be well observed. Park and Choe [18] have proposed a 20-cell stack dynamic model considering the temperature and two-phase effects. The temperature non-homogeneity is observed in simulation especially at the first and last 4 cells in the stack.

In this paper, a one-dimensional, dynamic, multi-physical fuel cell stack model is presented. This model is validated temporally and spatially against a commercial 1.2 kW fuel cell stack. From the presented model, the fuel cell dynamic behaviours are analysed through different domains. The fuel cell stack non-homogeneity is discussed and then a reduction method for fuel cell stack modelling is proposed. This spatially reduced model can be simulated much faster than the original model keeping the same accuracy at the same time. The original model and the reduced model can be used for real-time simulation or hardware-in-the-loop applications [19].

2. Multi-physic fuel cell stack dynamic model

The mechanistic fuel cell stack dynamic model presented in this paper is a generalized multi-physical, multi-cells PEM (proton

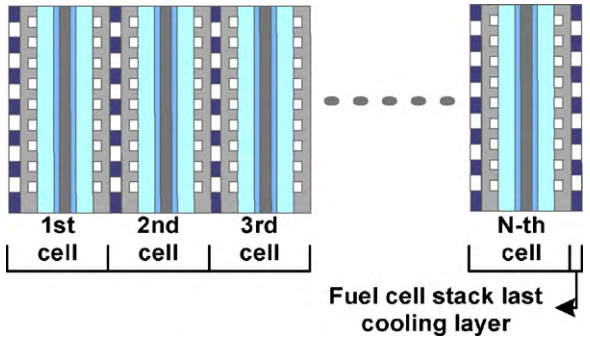

Fig. 1. Fuel cell stack model structure.

exchange membrane) dynamic fuel cell model. The model covers 3 major physical domains in the fuel cell: electrical, fluidic and thermal. The entire stack model is obtained from stacking individual cells together, as in a real stack. The model is based on a previous work presented in [20], with a dynamic modelling improvement in the electrical domain. The model is briefly introduced in the following sections. For a more detailed model description and a fully model experimental validation, the reader can refer to Ref. [20].

2.1. Fuel cell stack model structure

The individual cell is modelled in three major physical domains that can be found in a fuel cell: electrical, fluidic and thermal. The entire fuel cell stack is modelled by stacking N individual cells together. Every single cell model in the stack has the same physical model equations, but has different boundary conditions. The boundary conditions of k th cell are obtained from the cell $k-1$ and the cell $k+1$, as presented in Fig. 1.

Using this stacking structure, not only the temporal phenomena in a fuel cell, but also the spatial physical phenomena can be obtained. A fuel cell stack is always composed of single cells and each cell do not always has the same boundary conditions. Thus, the spatial non-homogeneity can be investigated by using this kind of real stack model.

2.2. Improved cell electrical dynamic model

In the electrical domain, the electrochemical reaction takes place at the catalyst layer, where the electromotive potential and activation losses occur. The hydrogen molecule is broken into two protons and two electrons at the anode side and the protons migrate through the membrane to the cathode side where they combine with oxygen ions at the cathode catalyst layer to produce water. The proton migration through the membrane depends on the membrane water content. This migration creates the most significant resistive losses in the fuel cell.

In addition, at the cathode catalyst layer, the positive (protons) and the negative (electrons) charges form a capacitance layer at the interface of the reaction sites, generally known as the "double layer capacitance", leading to the dynamic effect in the electrical domain.

The single cell voltage output can be expressed as follows:

$$V_{\text{cell}} = E_{\text{cell}} - V_{\text{act}} - V_{\text{ohm}} \tag{1}$$

where E_{cell} is the single cell electromotive force (V), V_{act} the cell activation losses at catalyst layer (V) and V_{ohm} the cell resistive losses (V).

The cell electromotive force can be obtained from the Nernst equation ([21], p. 36):

$$E_{\text{cell}} = 1.229 - 0.85 \cdot 10^{-3}(T - 298.15) + \frac{R \cdot T}{2F} \ln(\sqrt{P_{O_2}} \cdot P_{H_2}) \tag{2}$$

where T is the temperature of the cell (K), P_{O_2} the oxygen pressure (atm) at the cathode catalyst layer interface, P_{H_2} the hydrogen pressure (atm) at the anode catalyst layer interface, R the ideal gas constant ($8.314\,\text{J mol}^{-1}\,\text{K}^{-1}$) and F the Faraday constant ($96{,}485\,\text{C mol}^{-1}$).

It should be noted that, the gas pressures used in (2) are the gas pressures at the catalyst interface. These pressures are not the gas pressures in the supply channels. In reality, the electromotive force generation occurs in the catalyst layer. The pressures used in the OCV computation should be the pressure in catalyst layer of the reactants. The reactants pressures in gas channels are not equal to those at catalyst layer interface when the fuel cell is running. This is because the mass transport in GDL yields the individual pressure drop of each reactant. These mass transport losses are well taken into account in the present model, since the reactant pressures used in Eq. (2) are the pressures at the catalyst layer interface from GDL fluidic model introduced hereafter. Thus, the gas transport losses into the GDL, generally known as "concentration losses" are implicitly taken into account in the fluidic model in the following section and do not appear in (1). It should also be noted that, the Nernst equation used for fuel cell OCV calculation in the present model does not take into account the hydrogen crossover phenomenon. The hydrogen crossover can lead to a lower OCV observed in the real stack. Thus, the OCV calculated from the model is a little higher than the real OCV observed in the fuel cell stack. However, the fuel cell voltage and its OCV are also influenced by many other physical factors, such as temperature, gas pressures, and membrane resistance. Thus this OCV difference due to the assumption would not be seen significantly in the simulation results. Furthermore the hydrogen crossover in fuel cells is highly dependent on the fuel cell utilization time and membrane distortion, which can hardly be considered in a fuel cell mechanistic model. Thus in the present model the hypothesis that there is no hydrogen crossover was kept.

The cell static activation losses η_{act} (V) can be obtained from the Butler–Volmer potential equation ([22], p. 71):

$$i = i_0 \cdot S\left(e^{\frac{\alpha n F}{RT}\eta_{\text{act}}} - e^{\frac{-(1-\alpha)nF}{RT}\eta_{\text{act}}}\right) \tag{3}$$

where i is the stack current (A), S the catalyst layer section area (m^2), n the number of electrons involved in the reaction, α the symmetry factor and i_0 the exchange current density (A m^{-2}).

When η_{act} is small, Eq. (3) can be simplified by a linear equation:

$$\eta_{\text{act}} = \frac{RT}{nF} \cdot \frac{i}{i_0 S} \tag{4}$$

When η_{act} is large, Eq. (3) becomes the well-known Tafel equation:

$$\eta_{\text{act}} = \frac{RT}{\alpha n F} \ln\left(\frac{i}{i_0 S}\right) \tag{5}$$

The dynamic activation losses voltage V_{act} (V) due to the "double layer effect" in the electrical domain can be then expressed [23]:

$$\frac{\text{d}}{\text{d}t} V_{\text{act}} = \frac{i}{C_{\text{dl}}}\left(1 - \frac{1}{\eta_{\text{act}}} V_{\text{act}}\right) \tag{6}$$

where C_{dl} is the single fuel cell double layer capacitance (F).

The cell resistive losses V_{ohm} are mainly due to the membrane resistance. These losses can be obtained by computing the membrane resistance and the Joule's law:

$$V_{\text{ohm}} = R_{\text{mem}} \cdot i = \frac{i}{S} \int_0^{\delta_{\text{mem}}} r\,(T_{\text{mem}}, \lambda(z))\,\text{d}z \tag{7}$$

where δ_{mem} is the membrane thickness (m) and $r(T, \lambda(z))$ the membrane local resistivity (Ω m).

From the local water content of the membrane $\lambda(z)$ given as a function of the position on the z-axis (modeling axis) and the temperature of the membrane T_{mem} (K), the membrane resistivity

(Ω m) expression was investigated experimentally and published by Springer et al. in [24]:

$$r = \begin{cases} \dfrac{e^{\left[1268\cdot\left(\frac{1}{T_{mem}}-\frac{1}{303}\right)\right]}}{0.1933} & \text{if} \quad 0 < \lambda(z) \le 1 \\ \dfrac{e^{\left[1268\cdot\left(\frac{1}{T_{mem}}-\frac{1}{303}\right)\right]}}{0.5193\cdot\lambda(z)-0.326} & \text{if} \quad \lambda(z) > 1 \end{cases} \tag{8}$$

2.3. Cell fluidic dynamic model

In the fluidic domain, the supplied gases (hydrogen, air or oxygen) enter the gas channels of each cell in parallel. The hydrogen at the anode side and the oxygen at the cathode side migrate through the gas diffusion layer (GDL) to reach the anode and cathode catalyst sites. The produced water migrates into the gas channels in vapour or liquid form.

The migration of gases through the GDL is mostly due to the concentration gradient at the two sides of the GDL. At the same time, the gas flow in the channels leads to mechanical losses (head losses). All these phenomena lead to a pressure drop along the channels. The same phenomena can be also found in the cooling channels in each cell, but the pressure drop, in this case, is only due to mechanical losses of the coolant fluid.

The water balance in the membrane is a key factor of the fuel cell optimal operation. The water flow through the polymer membrane is mostly due to the electroosmotic and back diffusion phenomena.

The fluidic dynamic response of the fuel cell is generally due to the gas pressure dynamics in the channels (cooling, cathode and anode) which are given by the mass balance equation:

$$\frac{M_{gas}V_{Ch}}{RT}\left(\frac{d}{dt}P_{Ch}\right) = \sum_{in/out}^{Ch} q_{fluid} \tag{9}$$

where V_{ch} is the volume of the channels (m^3), M_{gas} is the gas molar mass ($kg\,mol^{-1}$), P_{cv} is the gas pressure in the channels (Pa) and q_{fluid} is the fluid mass flow ($kg\,s^{-1}$) entering or leaving the channels.

The flows through the gas supply channels are considered to be laminar flows. Thus the gas pressure drop in the channels due to mechanical losses can be expressed using the Darcy–Weisbach equation [25]:

$$\Delta P = \frac{64}{Re}\cdot\frac{\rho_{ch}L}{2D_{hydro}}V_S^2 \tag{10}$$

where D_{hydro} is the channels hydraulic diameter (m), V_s the mean fluid velocity in the channels ($m\,s^{-1}$), ρ_{ch} the channels gas density ($kg\,m^{-3}$), L the length of the channel (m) and Re, the fluid Reynolds number.

The Reynolds number can be calculated as [25]:

$$Re = \frac{\rho_{ch}V_S D_{hydro}}{\mu_{gas}} \tag{11}$$

where μ_{gas} is the fluid dynamic viscosity (Pa s)

From the ideal gas law, the gas density ρ_{ch} ($kg\,m^{-3}$) in the fuel cell channels can be obtained from the channels temperature T_{ch} (K) and the gas pressure P_{ch} (Pa) in the channels:

$$\rho_{ch} = \frac{M_{gas}P_{ch}}{RT_{ch}} \tag{12}$$

The mean fluid velocity can be calculated as follows:

$$V_s = \frac{q_{fluid}}{\rho_{ch}S} \tag{13}$$

where S is the channels section area (m^2).

From Eqs. (10)–(13), the gas mass flow rate at the inlet and the outlet of the channels can be obtained:

$$\begin{aligned} q_{inlet} &= k_f P_{ch}(P_{inlet} - P_{ch}) \\ q_{outlet} &= k_f P_{ch}(P_{outlet} - P_{ch}) \end{aligned} \tag{14}$$

The coefficient k_f is independent to the pressures:

$$k_f = \frac{S D_{hydro}^2 M_{gas}}{32 L R \mu_{gas} T_{ch}} \tag{15}$$

The gas mass flow rate ($kg\,s^{-1}$) through the gas diffusion layers is directly related to the stack current, as described in the following equations:

$$q_{O_2} = \frac{M_{O_2} i}{4F} \tag{16}$$

$$q_{H_2} = -\frac{M_{H_2} i}{2F} \tag{17}$$

$$q_{H_2O,produced} = -\frac{M_{H_2O} i}{2F} \tag{18}$$

The multi-gas diffusion of each species (oxygen, hydrogen, nitrogen and water vapor) through the gas diffusion layers (GDL) can be described by the Stefan–Maxwell equation [26]:

$$\Delta P_i = \frac{\delta_{GDL} RT}{P_{tot} S}\sum_{j\neq i}\frac{P_i\cdot(q_j/M_j) - P_j\cdot(q_i/M_i)}{D_{ij}} \tag{19}$$

where δ_{GDL} is the GDL thickness (m), S is the GDL layer section area (m^2), P_{tot} is the mean gas total pressure (Pa) in the GDL layer, M is the gas molar mass ($kg\,mol^{-1}$), j stands for species other than species i, and D_{ij} is the binary diffusion coefficient between the species i and j ($m^2\,s^{-1}$).

In the membrane layer, the water content can be expressed as [22]:

$$\lambda = \begin{cases} 0.0043 + 17.81\cdot a_{H_2O} - 39.85\cdot a_{H_2O}^2 + 36\cdot a_{H_2O}^3 & [0 < a_{H_2O} \le 1] \\ 14 + 1.4\cdot(a_{H_2O} - 1) & [1 < a_{H_2O} \le 3] \end{cases} \tag{20}$$

where a_{H_2O} is the water activity, calculated from the partial water vapor pressure P_{H_2O} (Pa) and the water saturation pressure P_{sat} (Pa):

$$a_{H_2O} = \frac{P_{H_2O}}{P_{sat}} \tag{21}$$

The water balance in the membrane layer can be described by two different phenomena: the *electro-osmosic drag* described by Eq. (22), and the *back diffusion* described by Eq. (23)[22].

$$J_{drag} = \frac{n_{sat}}{11}\cdot\frac{\lambda_A + \lambda_C}{2}\cdot\frac{i}{2F}\cdot M_{H_2O} \tag{22}$$

$$J_{back\_diff} = \frac{\rho_{dry}}{M_n}\cdot D_\lambda\cdot\frac{\lambda_A - \lambda_C}{\delta_{mem}}\cdot S\cdot M_{H_2O} \tag{23}$$

where $n_{sat} = 22$ is the electro-osmotic drag coefficient for maximum hydration condition, ρ_{dry} is the dry density of the membrane ($kg\,m^{-3}$),D_λ the mean water diffusion coefficient in the membrane ($m^2\,s^{-1}$), δ_{mem} is the membrane thickness (m), λ_A is the membrane water content at the anode side, λ_C is the membrane water content at the cathode side and M_n the equivalent mass of the membrane ($kg\,mol^{-1}$).

The total water mass flow ($kg\,s^{-1}$) through the membrane can be then expressed as follows:

$$q_{H_2O,net} = J_{drag} + J_{back\_diff} \tag{24}$$

The net membrane water mass flow can be computed from Eqs. (22)–(24):

$$q_{H_2O,net} = k_{EO}(\lambda_A + \lambda_C) + k_{BD}D_\lambda(\lambda_A - \lambda_C) \tag{25}$$

where k_{EO} and k_{BD}, are two coefficients independent to the membrane water content:

$$k_{EO} = \frac{n_{sat} M_{H_2O} i}{44 F}$$
$$k_{BD} = \frac{\rho_{dry} SM_{H_2O}}{\delta_{mem} M_n} \quad (26)$$

2.4. Cell thermal dynamic model

During the fuel cell operation, heat is generated due to entropy changes from the electrochemical reaction. In parallel, the electrical activation losses and resistive losses contribute also to the total heat generation. The generated heat is conducted, by conduction or fluid convective flow, through different layers in the cell, and then can be removed, by forced convection with coolant in the cooling channels or by radiation and by natural convection between the fuel cell bipolar plates surface and ambient air.

The thermal dynamic response of a fuel cell depends on the thermal capacity of each layer in the cell. This dynamic can be generally described in a general form as:

$$(\rho V C_p)\frac{dT_{CV}}{dt} = \underbrace{\dot{Q}_{cond}}_{\text{conduction}} + \underbrace{\dot{Q}_{forced\_conv}}_{\text{forced convection}} + \underbrace{\dot{Q}_{nat\_conv\_radia}}_{\text{natural convection and radiation}} + \underbrace{\dot{Q}_{mass}}_{\text{convective mass flow}} + \underbrace{\dot{Q}_{sources}}_{\text{internal sources}} \quad (27)$$

where ρ is the mean layer volume density ($kg\,m^{-3}$), V is the layer volume (m^3), C_p is the layer thermal capacity ($J\,kg^{-1}\,K^{-1}$) and $\dot{Q}$ stands for the different types of heat flows entering or leaving the layer volume ($J\,s^{-1}$): conduction, forced convection, natural convection, radiation, convective mass flow and internal sources of heat.

The heat between solid materials layers in the fuel cell stack is transferred by conduction according to the Fourier's Law [27]:

$$\dot{Q}_{cond} = \frac{\lambda S_{contact}}{\delta}(T_{layer1} - T_{layer2}) \quad (28)$$

where λ is the material thermal conductivity ($W\,m^{-1}\,K^{-1}$), S is the contact area (m^2) and δ the material thickness (m).

The heat exchanges between the solid material and the fluid flow (forced convection), such as cooling flow, cathode and anode flows, can be described by the Newton cooling law [27]:

$$\dot{Q}_{forced\_conv} = h_{forced} S_{contact}(T_{fluid} - T_{solid}) \quad (29)$$

where h_{forced} is the forced convection heat transfer coefficient ($W\,m^{-2}\,K^{-1}$).

In addition, considering the fuel cell bipolar plate size and the number of cells in one stack, the heat exchanges due to the natural convection and radiation should be considered:

$$\dot{Q}_{nat\_conv\_radia} = h_{nat\_radia} S_{ext}(T_{amb} - T_{solid}) \quad (30)$$

where h_{nat_radia} is the combined natural convection and radiation heat transfer coefficients ($W\,m^{-2}\,K^{-1}$), S_{ext} is the external area of the bipolar plate (m^2), and T_{amb} is the external environment temperature (K).

When the fuel cell stack is operating, different fluid flows can be found in the cell: gas transports through the gas diffusion layers, the water flow through the membrane, the cooling flows entering or leaving the channels, etc. These convective mass transports bring an additional heat flow into each layer in the fuel cell:

$$\dot{Q}_{mass} = \left[\sum_{fluid}(q_{fluid} \cdot C_{p,fluid})\right](T_{fluid} - T_{layer}) \quad (31)$$

Table 1
Ballard Nexa fuel cell stack.

Stack configuration	
Fuel cell type	PEMFC dead-end mode
Cell number in stack	47 cells
Fuel supply	99.99% dry hydrogen
Fuel supply pressure	70–1720 kPa
Air supply	Air blower
Cooling	Air fan cooled
Mass	13 kg
Life time	1500 h
Operating conditions and characteristics	
Rated power output	1.2 kW
Current at rated power	46 A
Voltage at rated power	26 V
Voltage range	22–50 V
Ambient temperature	3–40 °C
Relative humidity	0–95 %
Heat dissipation	1.6 kW

When the fuel cell stack produces electricity from the electrochemical reactions, heat is also generated at the same time. The main heat sources in the fuel cell are due to the irreversible losses in the electrochemical reaction and the resistive losses from the membrane resistance.

The main irreversible losses occur at the cathode catalyst layer due to entropy change in the reaction and the activation losses. These losses can be calculated as follows:

$$\dot{Q}_{source1} = \underbrace{-i \cdot \frac{T\,\Delta S}{2F}}_{\text{entropy change part}} + \underbrace{i \cdot V_{act}}_{\text{activation part}} \quad (32)$$

where ΔS is the entropy change ($J\,mol^{-1}\,K^{-1}$) during the electrochemical reaction.

The fuel cell internal resistance is generally due to the polymer membrane resistance. When the protons pass through the fuel cell membrane heat is generated from resistive losses due to the membrane protonic resistance:

$$\dot{Q}_{source2} = i^2 \cdot R_{mem} \quad (33)$$

2.5. Experimental validation

The proposed multi-physical fuel cell stack model has been validated temporally and spatially with a commercial Ballard Nexa 1.2 kW 47 cells fuel cell stack. The Nexa stack is supplied with pure hydrogen and compressed air by means of a blower. The anode channels are working in "dead-end" configuration. The entire stack is cooled by forced air flow in the cooling channels.

The fuel cell stack configurations and operation conditions are listed in Table 1.

For more detailed stack geometry parameters and physical properties, including channels length, layer thickness, material thermal conductivity and capacity, material density, please refer to Ref. [20].

During the experimental procedure, the stack global physicals, such as stack current, stack voltage, air outlet temperature, cooling fan speed, has been obtained from the fuel cell stack monitoring software provided by Ballard Company. In order to validate at same time the stack model spatial physical distribution of cell voltage and temperature, 2 additional devices has been used (see Fig. 2). For the measurement of individual cell voltage, a group of differential voltage sensors has been added to the stack, the measurement is done in National Instrument LabView environment. For the measurement of individual cell temperature during operating, an infrared camera has been used to capture

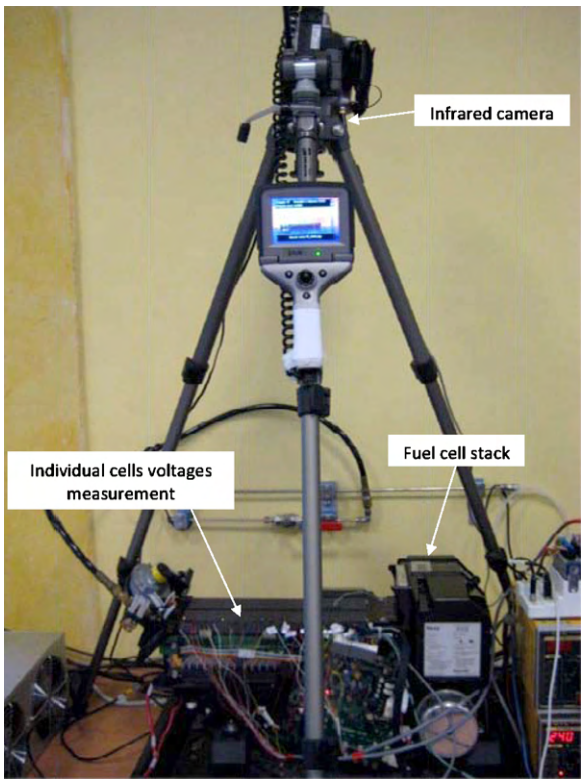

Fig. 2. Photo of the test bench.

in continuous the cell temperature evolutions in the operating stack.

The experimental stack current profile between 2 A and 45 A during about 1300 s (21 min 40 s) is presented in Fig. 3. The same stack current has been applied to the proposed fuel cell stack model, in order to compare the simulation result with those of experimentation.

As illustrated in Fig. 4, the 47 cells stack voltage can be predicted by the model with a very good accuracy in the hole time range. In order to see more clearly the difference between the experimental and simulation results, the relative error analysis is presented in Fig. 5. It can be conclude that during the most part of time range, the relative error of the presented model is less than 5%. The maximum relative error observed does not exceed 10%. It has to be noted that, the stack voltage from the model is obtained by adding the 47 individual cell voltages in the fuel cell stack model. Thus, the model accuracy can be proved.

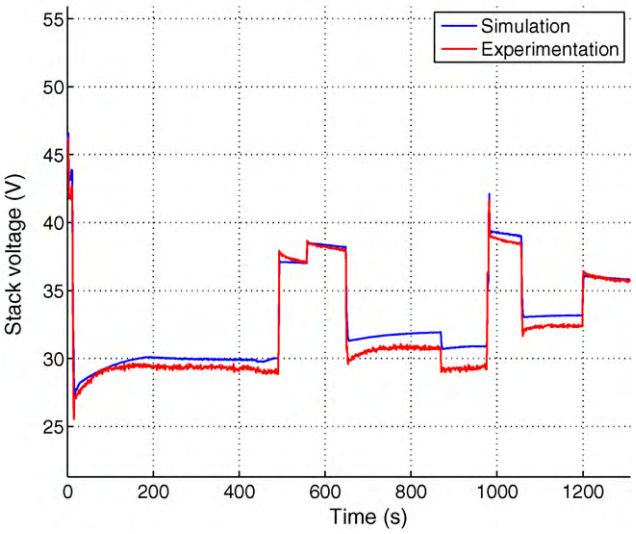

Fig. 4. Fuel cell stack voltage.

In addition, because every single cell in the stack has been modelled individually, the single cell behaviour can be obtained from the model. The 47 cells individual voltage distribution in the stack at 507 s is given in Fig. 6. It can be concluded that the cell individual voltage can also be well predicted spatially by the model.

The single cell temporal behaviour in the stack is shown in Fig. 7. The middle cell (24th cell) voltage temporal result from the experimentation has been compared to the model result. Thanks to the model stacking structure, beside the stack overall voltage, the single cell voltage in the stack can also be predicted accurately.

Fig. 8 shows the cathode air outlet temperature dynamic profile. The experimental data measured by a temperature sensor at the cathode channels outlet has been compared to the model predicted results at the same position. From a large range of temperature, the model results demonstrate a very good temporal dynamic accuracy with the measured results. To state out the relative error of model prediction, an error analysis is introduced in Fig. 9 and it can be seen that the temperature prediction error is less than 5%.

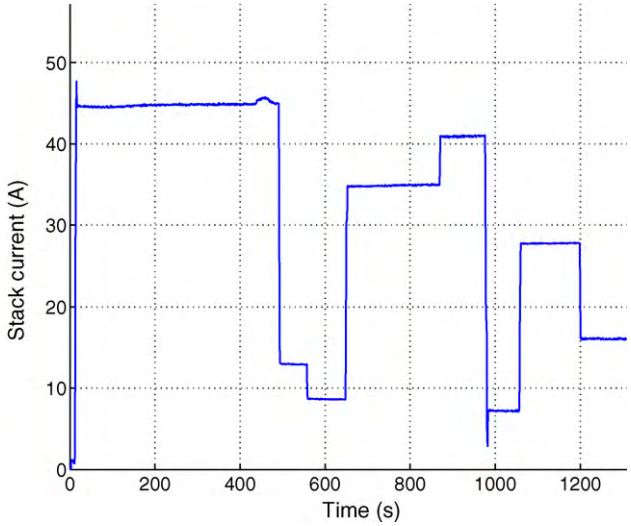

Fig. 3. Stack current profile.

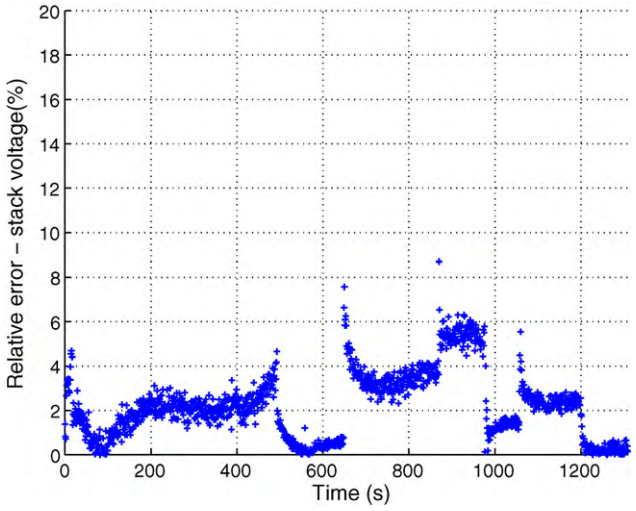

Fig. 5. Voltage relative error analysis between the model and the experimentation.

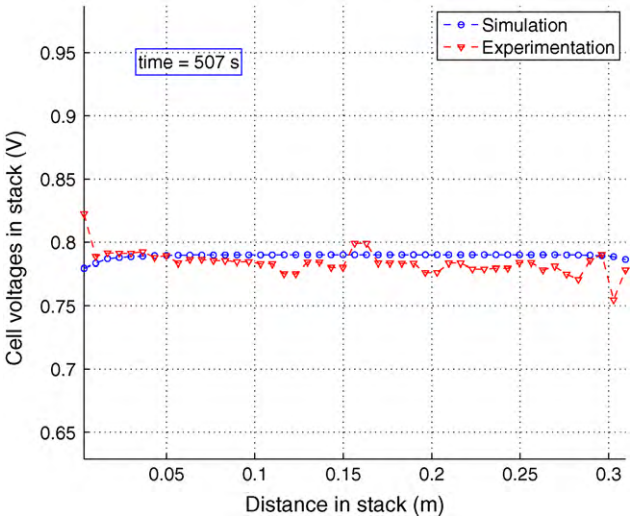

Fig. 6. Individual cell voltages at 507 s.

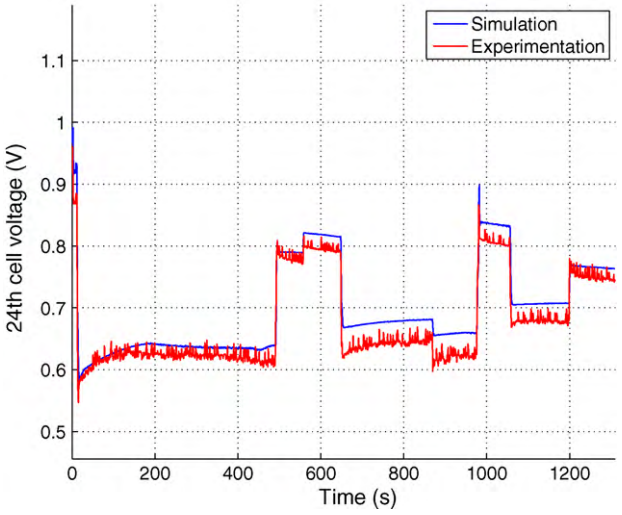

Fig. 7. 24th cell voltage in the stack.

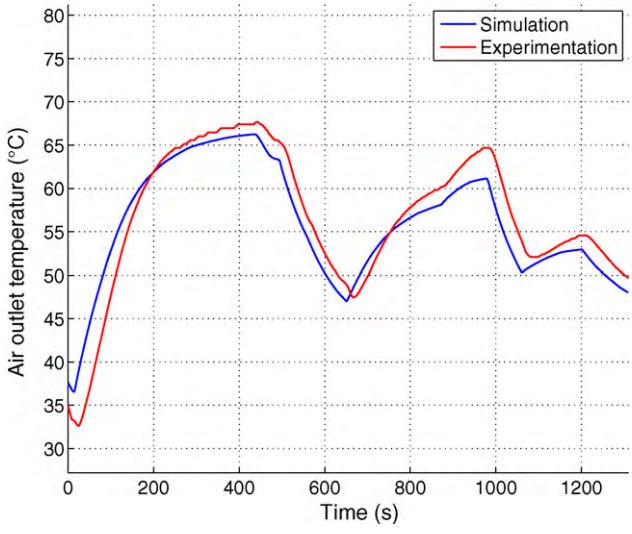

Fig. 8. Cathode air outlet temperature (stack temperature).

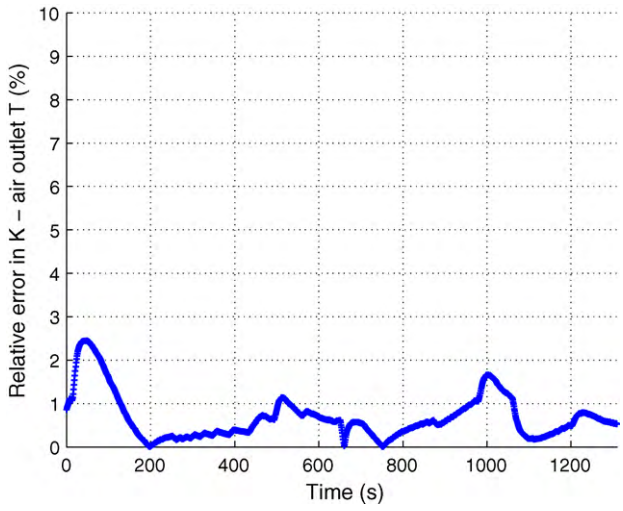

Fig. 9. Air outlet temperature relative error analysis between the model and the experimentation

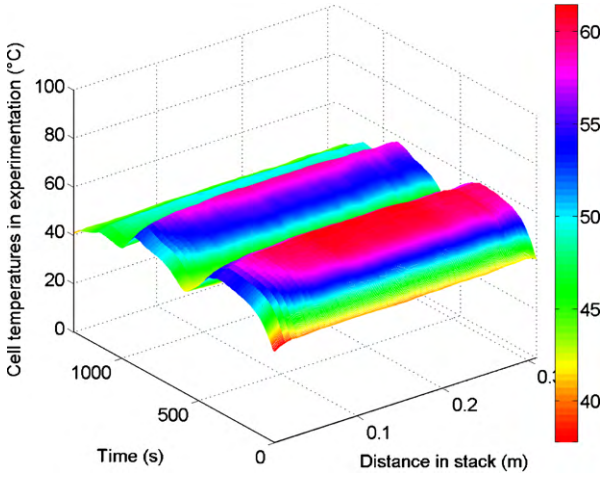

Fig. 10. Measured stack temperatures variation.

As in the electrical domain, the individual cell temperatures can be obtained from the proposed model. The spatial and temporal evolutions of the 47 cells in the stack are shown in Fig. 10 (measured) and Fig. 11 (simulated). A detailed comparison at 137 s is

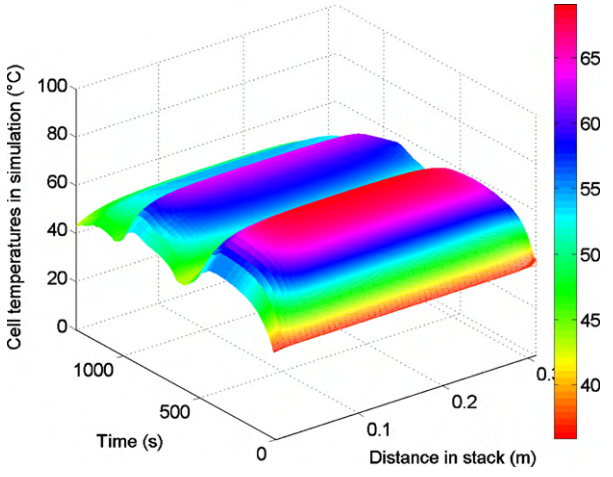

Fig. 11. Simulated stack temperatures variation.

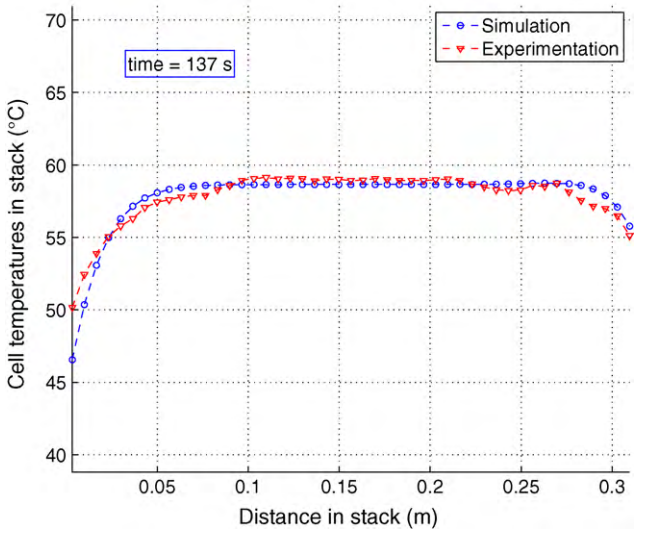

Fig. 12. Individual cell temperatures at 137 s.

given in Fig. 12. Again, the results show good agreements between the experimental and simulation data.

The proposed model can also predict many other stack physicals in the stack. For example, the prediction of the cathode air inlet pressure from the air compressor is given in Fig. 13. In addition, some non-measurable physicals, such as membrane water mass flows, reactant pressure at the catalyst interface, can be obtained from the fuel cell stack model. For, example, due to the membrane thickness, the membrane water contents, which is a key factor of the fuel cell performance, cannot be measured directly. These physicals can somehow be obtained from the model, as shown in Fig. 14: the middle cell (24th cell) temporal membrane water content profile.

From the experimental results, it can be concluded that the proposed model can predict the fuel cell stack temporal and spatial behaviours correctly.

2.6. Improved electrical model comparison and discussion

The presented model in the section above is based on the work in [20]. However, compared to the model presented in [20], electrical model has been improved.

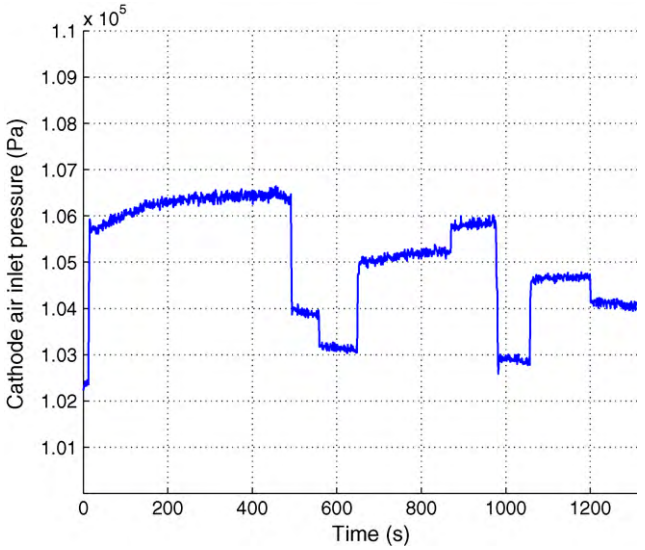

Fig. 13. Cathode air inlet pressure.

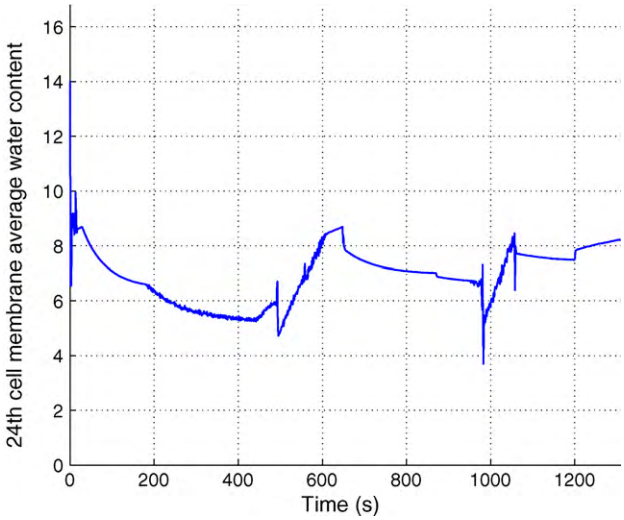

Fig. 14. 24th cell membrane water content.

In the present model, the activation loss formula has been changed from empirical equation to Butler–Volmer mechanistic equation. In addition, the dynamic double layer capacity effect has been considered now in the present model.

In order to demonstrate the influence of these improvement on the model results, a comparison of stack voltage behaviour between model in [20] and present improved model is performed hereafter.

A step current from 35 A to 15 A were applied in the both models as shown in Fig. 15.

Fig. 15 shows the stack voltage response from the model in [20] and the model in this paper. From the figure, it can be conclude that, as the electrical model in [20] is a steady-state model, the dynamic response due to the double layer capacity can not be predicted. By the results of present model, this dynamic phenomenon can last 1 s. Thus it is relatively significant in the stack voltage dynamic behaviour. A detailed analysis of this dynamic will be presented in the following section.

In the other side, the steady-state value of stack voltage has a slight difference between two models. This difference is due to the different equation used for activation loss expression. In [20], an empirical equation is used. Four empirical parameters need to be identified from specific fuel cell polarization curve. In the present model, the activation loss is obtained from mechanistic Butler–Volmer equation, thus the model does not need to be calibrated from empirical data.

From the points stated out above, it can be conclude that, the present model has an important improvement in electrical domain compare to the model in [20].

3. Fuel cell multi-physical dynamic phenomena

As described in the modelling sections, different dynamic phenomena exist in electrical, fluidic and thermal domains. In the electrical domain, the dynamic is due to the double layer capacity at the catalyst interface. In the fluidic domain, the dynamic is due to the channels volume and water balance through the cathode and the anode. In the thermal domain, the dynamic is due to the heat generation and the heat capacity of materials.

Although these dynamics are all first order dynamic, their temporal behaviour are quite different compared to each other. In order to have a general understanding of these dynamics, different theory analyses are performed in the following sections. The aim of these analyses is to obtain the first order dynamic “time constant”

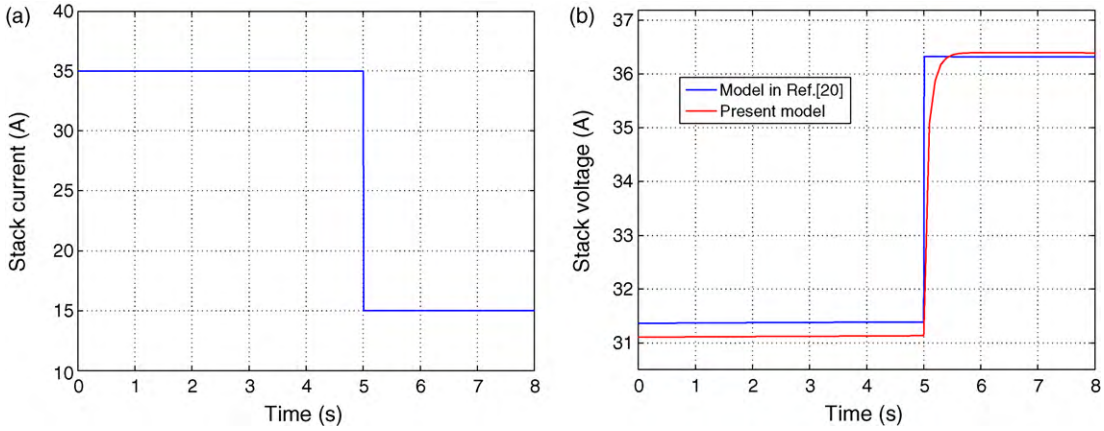

Fig. 15. (a) Step current from 35 A to 15 A. (b) Comparison between the model and the proposed model in [20].

analytical expression in each domain as a function of the fuel cell stack parameter.

3.1. First order dynamic system: general form and time constant

In the Laplace domain, a general first order system can be described as follows:

$$Y(s) = \frac{1}{1+\tau \cdot s} X(s) \tag{34}$$

where $X(s)$ is the system input signal, $Y(s)$ is the system output signal, τ is the first order system time constant and s is the Laplace variable.

In addition, if $X(s)$ is a constant step signal, the final steady-state value of the $Y(s)$ is the same than the step amplitude, which is noted Y_{Final}. Thus, Eq. (34) can be changed as:

$$Y(s) = \frac{1}{1+\tau \cdot s} \cdot \frac{Y_{\text{Final}}}{s} \tag{35}$$

Eq. (35) in the Laplace domain can be transferred to the time domain, in the form of the following equation:

$$\tau \cdot \frac{\mathrm{d}}{\mathrm{d}t} y(t) + y(t) = y_{\text{Final}} \tag{36}$$

where $y(t)$ is the temporal response of the physical system and y_{Final} is the system final steady-state value.

Thus, if a first order dynamic physical system can be arranged to the form of Eq. (36), the expression of the time constant of the system can be easily deduced. It must be noted that the first order dynamic system response time is about 4 times of the system time constant value.

3.2. Electrical dynamic: double layer capacitance effect

In the electrical domain, the dynamic effect is due to the double layer capacitance in the fuel cell catalyst layer.

From Eqs. (1), (5) and (6), the cell voltage dynamic can be expressed:

$$\frac{\mathrm{d}V_{\text{cell}}}{\mathrm{d}t} = -\frac{\mathrm{d}V_{\text{act}}}{\mathrm{d}t} = \frac{i}{C_{\text{dl}}} \left(\frac{E_{\text{cell}} - V_{\text{cell}} - V_{\text{ohm}}}{\eta_{\text{act}}} - 1 \right) \tag{37}$$

The cell voltage steady-state expression can be described as follows:

$$V_{\text{cell\_Final}} = E_{\text{cell}} - V_{\text{ohm}} - \eta_{\text{act}} \tag{38}$$

Thus, the following equation form can be obtained:

$$\frac{\eta_{\text{act}} \cdot C_{\text{dl}}}{i} \cdot \frac{\mathrm{d}V_{\text{cell}}}{\mathrm{d}t} + V_{\text{cell}} = V_{\text{cell\_Final}} \tag{39}$$

The time constant expression in the fuel cell electrical domain is:

$$\tau_{\text{electrical}} = \frac{C_{\text{dl}} R T}{\alpha n F i} \ln\left(\frac{i}{i_0 S} \right) \tag{40}$$

In the Ballard 1.2 kW fuel cell stack case, the double layer capacitance of the single cell is measured using experimental method. The value of this capacitance is about 150 F m^{-2}. From the Nexa fuel cell stack characteristic data given in [20], the electrical time constant in the Nexa fuel cell stack is found to be around 0.16 s. Thus, the electrical transient time is about 0.64 s when current step occurs.

In order to visualize the cell voltage electrical dynamic effect, 2 different current profiles have been applied to the Ballard 1.2 kW fuel cell stack.

The first test current profile is shown in Fig. 16. A step change from 0 A to 35 A is done at 10 s, and followed another step change from 35 A to 15 A at 30 s.

The corresponding middle cell (24th cell in stack) voltage dynamic responses at 10 s and 30 s are shown in Figs. 17 and 18. From the figures, it can be concluded that the electrical transient time is about 0.6 s, which means that the electrical time constant for the cell is about 0.15 s for this current profile.

The second test current profile is shown in Fig. 19.

The cell voltage dynamic response at 30 s is illustrated in Fig. 20. The transient time can be approximated

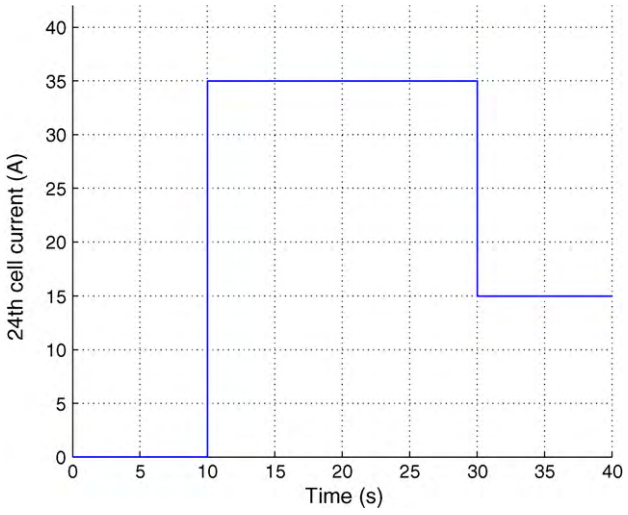

Fig. 16. 1st stack current test profile (during 40 s).

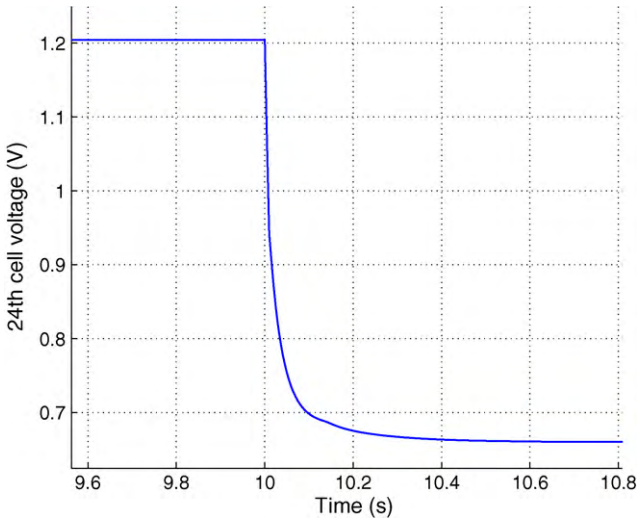

Fig. 17. 1st test: middle cell voltage dynamic response at 10 s.

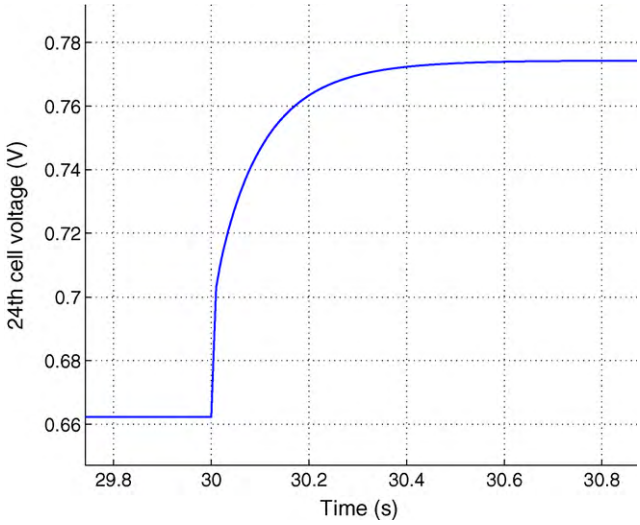

Fig. 18. 1st test: middle cell voltage dynamic response at 30 s.

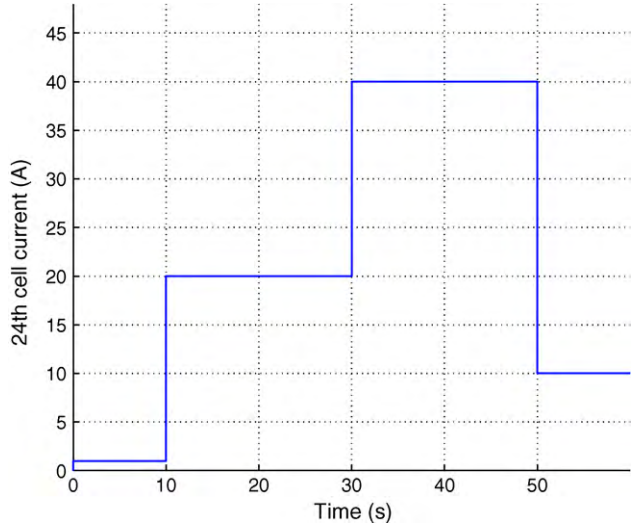

Fig. 19. 2nd stack current test profile (during 60 s).

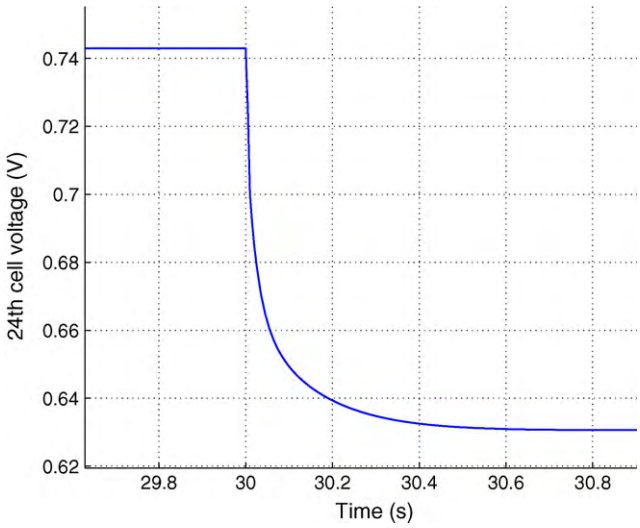

Fig. 20. 2nd test: middle cell voltage dynamic response at 30 s.

to 0.7 s, which gives a time constant value around 0.175 s.

These values are in agreement with the one found using the analytical equation given in (40).

3.3. Fluidic dynamic: gas channels dynamic effect

In the fluidic domain, the first kind of dynamic is due to the gas supply channels volume. Generally, in the fuel cell, in the cooling and cathode side, the cooling and cathode channels inlet mass flow rates and outlet pressures are known as they can be found using geometrical parameters. The anode channels inlet pressure is also known.

From Eqs. (9)–(14), the gas channels dynamic can be expressed:

$$\frac{dP_{ch}}{dt} = \frac{RT}{MV}(q_{inlet} + k_f \cdot P_{ch}(P_{outlet} - P_{ch})) \tag{41}$$

In (41), the gas inlet mass flow rate and channels outlet pressure are known.

Thus, the channels steady-state pressure expression can be calculated:

$$P_{ch\_Final} = P_{outlet} + \frac{q_{inlet}}{k_f P_{ch\_Final}} \tag{42}$$

It must to be noted that this channels pressure equation is in implicit form, because the steady-state channels pressure appears in both side of the equation.

From (41), the general first order system equation (36) can be approached:

$$\frac{MV}{RTk_f P_{ch}}\frac{dP_{ch}}{dt} + P_{ch} = \underbrace{P_{outlet} + \frac{q_{inlet}}{k_f P_{ch\_Final}}}_{P_{ch\_Final}} + \underbrace{\frac{P_{ch\_Final} - P_{ch}}{P_{ch}} \cdot \frac{q_{inlet}}{k_f P_{ch\_Final}}}_{\Delta\varepsilon} \tag{43}$$

Compared to the final desired form, an additional error $\Delta\varepsilon$ appears in (43). During the fuel cell operation, the fuel cell stack channels pressure variation P_{ch} is typically less than 5%:

$$\underbrace{\frac{P_{ch\_Final} - P_{ch}}{P_{ch}} \cdot \frac{q_{inlet}}{k_f P_{ch\_Final}}}_{\Delta\varepsilon} \leq 5\% \cdot \frac{q_{inlet}}{k_f P_{ch\_Final}} \tag{44}$$

Thus, compared to the steady-state channels pressure expression in (42), this error is quite small and then can be neglected. With this assumption, the cooling and cathode channels pressure

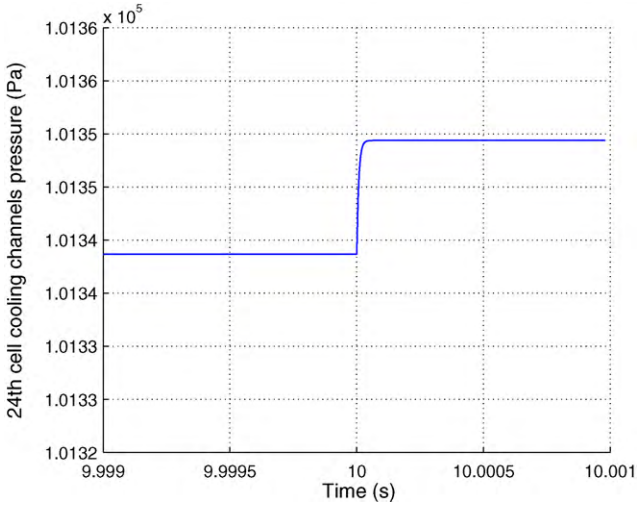

Fig. 21. 1st test: cooling channels pressure dynamic response at 10 s.

time constant in the fluidic domain can be obtained:

$$\tau_{\text{fluidic\_channels}} = \frac{32\,L^2\,\mu_{\text{gas}}}{D_{\text{hydro}}^2\,P_{\text{ch}}} \tag{45}$$

The similar mathematical method can be applied to the anode channels. The anode channels pressure time constant has the same form of Eq. (45).

In the Ballard 1.2 kW fuel cell stack, from the fuel cell gas supply channels geometry and gas properties given in [20], the cooling channels pressure time constant is found to be around 8.14 μs, the cathode channels pressure time constant is about 6.92 ms and the anode channels pressure time constant is about 25.1 ms. The anode time constant is much bigger than the one at the cathode side, because the anode supply channels are longer.

The time constants are validated in simulation. The first test stack current profile (Fig. 16) is applied. For the Ballard 1.2 kW fuel cell stack, the stack cooling air inlet mass flow rate depends linearly on the stack current. Thus, the cooling channels pressure dynamic responses at stack current changes are shown in Figs. 21 and 22.

From these figures, the transient time of the cooling dynamic is about 40 μs, thus the pressure time constant for cooling channels can be estimated to be 10 μs, which is very close to the theoretical time constant value found in (45).

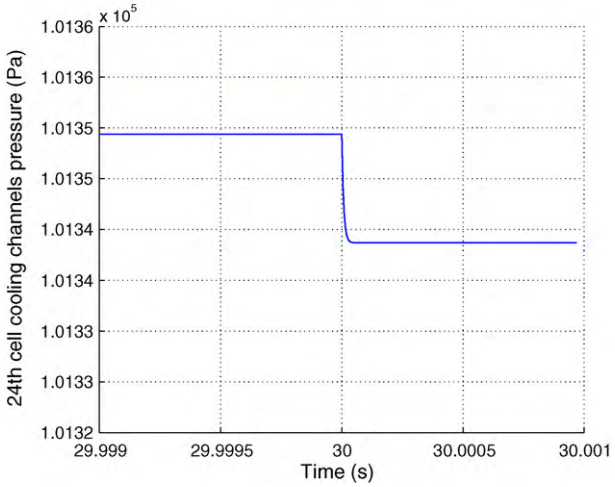

Fig. 22. 1st test: cooling channels pressure dynamic response at 30 s.

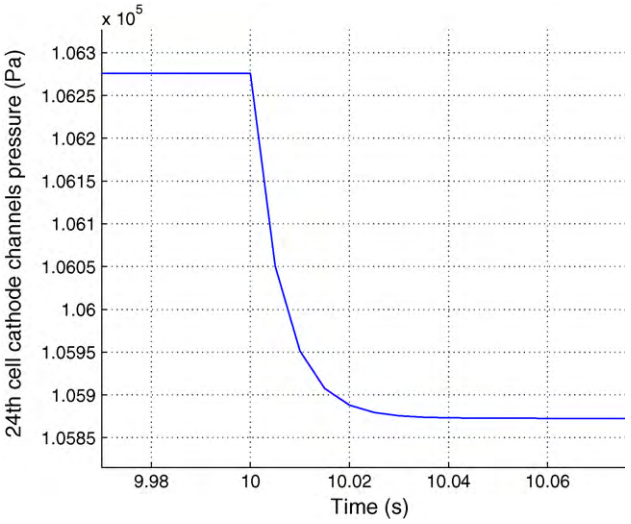

Fig. 23. 1st test: cathode channels pressure dynamic response at 10 s.

At each current step change, the cathode channels pressure dynamic response is given in Figs. 23 and 24. The corresponding transient time can be approximated to 30 ms which is still in the order of magnitude of the time constant calculated with (45).

At last, the anode channels pressure dynamic responses can be found in Figs. 25 and 26. The anode channels pressure has a relative long transient time, which is estimated to 0.12 s from the figures.

These values are in agreement with the ones found using the analytical equation given in (45).

3.4. Fluidic dynamic: membrane water diffusion effect

In the fluidic domain, another kind of dynamic exists: the water balance dynamic through the membrane.

The fuel cell type considered in this section is a cathode fully hydrated; anode dead-end mode and pure dry hydrogen supplied fuel cell, which is the most common fuel cell type. In the dead-end mode, the anode channels water presence is only due to the membrane water diffusion from the cathode to the anode. With the anode channels volume, the vapour pressure rises when the water flows into the anode channels through the membrane, and decreases when the water flows out. Thus, the membrane

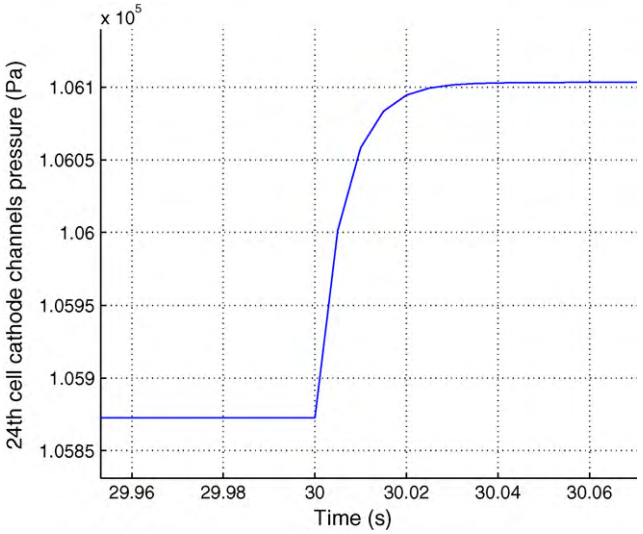

Fig. 24. 1st test: cathode channels pressure dynamic response at 30 s.

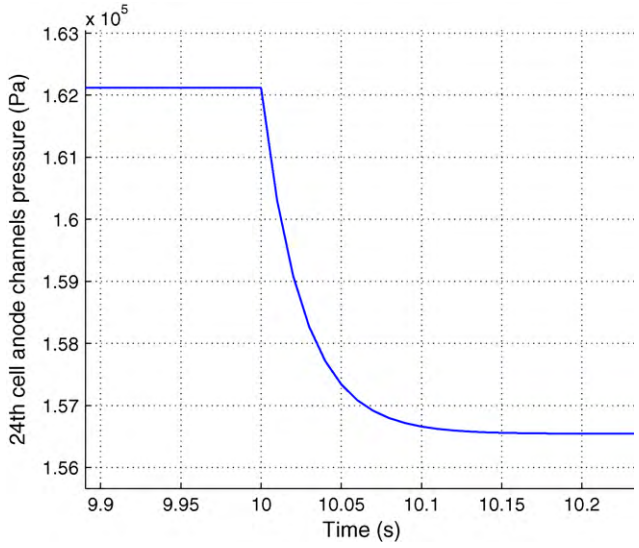

Fig. 25. 1st test: anode channels pressure dynamic response at 10 s.

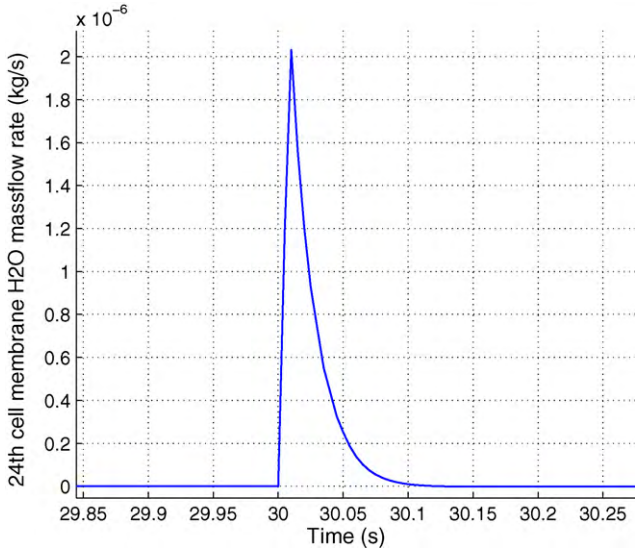

Fig. 27. 1st test: membrane water mass flow dynamic response at 30 s.

water dynamic is due to the membrane net water flow and the anode channels gas volume. The membrane net water flow can be calculated from the balance between the water vapour pressure difference at the cathode and the anode sides, and the stack current electro-osmotic drag.

From this consideration and using Eqs. (9) and (25), the following equation can be obtained:

$$\frac{M_{H_2O}\,V_{anode}}{RT}\cdot\frac{dP_{H_2O\_anode}}{dt} = -k_{EO}(\lambda_A+\lambda_C) - k_{BD}D_\lambda(\lambda_A-\lambda_C) \quad (46)$$

With the assumption that the fuel cell cathode side is always fully hydrated, the cathode side water content λ_C is constant.

To simplify (46), the derivative of anode side water vapour pressure $P_{H_2O\_anode}$ can be replaced by the derivative of the anode side water content λ_A, using a linear approximation for $a_{H_2O} < 1$, from Eqs. (20) and (21):

$$\frac{dP_{H_2O\_anode}}{dt} = \frac{P_{sat}}{9.5955}\frac{d\lambda_A}{dt} \quad (47)$$

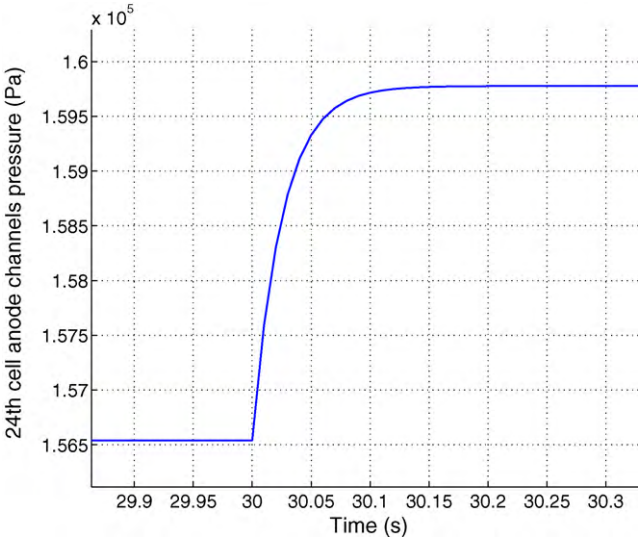

Fig. 26. 1st test: anode channels pressure dynamic response at 30 s.

From (46), the steady-state anode water content value can be calculated:

$$\lambda_{A\_Final} = \frac{k_{BD}D_\lambda - k_{EO}}{k_{BD}D_\lambda + k_{EO}}\lambda_C \quad (48)$$

Thus, the general form of the membrane water diffusion dynamic equation can be using Eqs. (46)–(48):

$$\frac{P_{sat}\,M_{H_2O}\,V_{anode}}{9.5955\,RT(k_{BD}D_\lambda + k_{EO})}\cdot\frac{d\lambda_A}{dt} + \lambda_A = \lambda_{A\_Final} \quad (49)$$

With the expressions of the k_{BD} and k_{EO}, the membrane water diffusion dynamic time constant in the fluidic domain can be obtained:

$$\tau_{fluidic\_mem} = \frac{P_{sat}\,V_{anode}}{9.5955RT\left(\frac{D_\lambda\,\rho_{dry}\,S}{\delta_{mem}M_n} + \frac{n_{sat}\,i}{44F}\right)} \quad (50)$$

With the Ballard 1.2 kW fuel cell stack using the nominal operating temperature 338.15 K, the maximum power current 40 A, the membrane properties [20] and membrane water contents, the membrane water dynamic time constant is approximated from 0.0082 s to 0.12 s.

The membrane water mass flows for several current steps are shown in the figures hereafter.

For the first test current profile (Fig. 16), the membrane water mass flow rate at 30 s is shown in Fig. 27. With a large current value and low stack temperature at start, the water diffusion transient time is about 0.1 s.

With the second test current profile (Fig. 19), the membrane water mass flow dynamic responses in the middle cell at 30 s and 50 s are shown in Figs. 28 and 29. From these figures, the corresponding transient time can be estimated between 0.06 s and 0.1 s, with different fuel cell operating conditions.

3.5. Thermal dynamic: stack thermal capacities

The fuel cell thermal dynamic is the most significant dynamic in the fuel cell stack. This kind of dynamic can be relatively long, because the cell components (bipolar plates, membrane, etc.) have large thermal capacities and volumes.

In a single fuel cell control volume in the middle of the stack, different thermal phenomenon can be identified: the internal heats sources due to the electrochemical process and stack current; the forced convection due to the cooling fluid mass flow; the natural

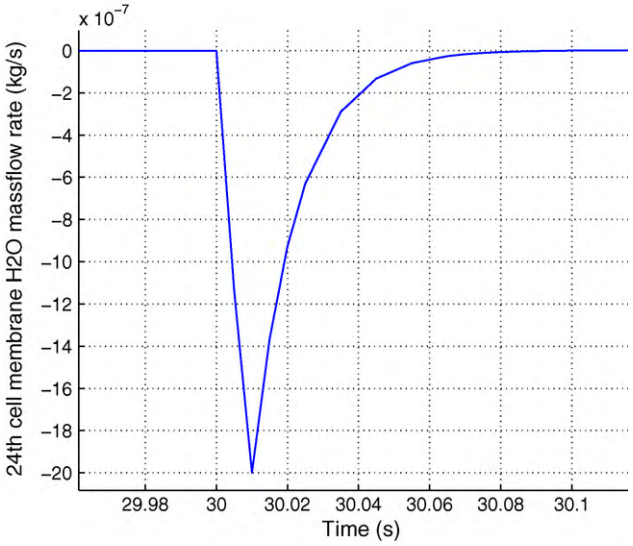

Fig. 28. 2nd test: membrane water mass flow dynamic response at 30 s.

convection and radiation due to the high temperature of the cell during operation. It has to be noted that, since the cells in the middle of the fuel cell stack have almost the same temperature, the conduction phenomena between the cells can be neglected.

From Eq. (27), the single cell level control volume thermal dynamic equation can be expressed:

$$\rho_{\text{cell}}\, V_{\text{cell}}\, C_p\, \frac{\mathrm{d}T_{\text{cell}}}{\mathrm{d}t} = \dot{Q}_{\text{sources}} + \dot{Q}_{\text{forced}} + \dot{Q}_{\text{nat\_radia}} \tag{51}$$

In Eq. (51), each of the heat flows $\dot{Q}$ should be expressed as a function of the T_{cell}.

In order to get the final linear system dynamic equation, the linearization methods for the fuel cell operating temperature interval (293.15–343.15 K) are applied to the internal heat sources equations.

From Eqs. (3)–(8), (32) and (33), the linear expression of the heat sources as a function of the cell temperature can be obtained:

$$\dot{Q}_{\text{sources}} = k_{\text{sources}}\, T_{\text{cell}} + i\,\eta_{\text{act}} + 4.2\, i^2\, k_{\text{mem}} \tag{52}$$

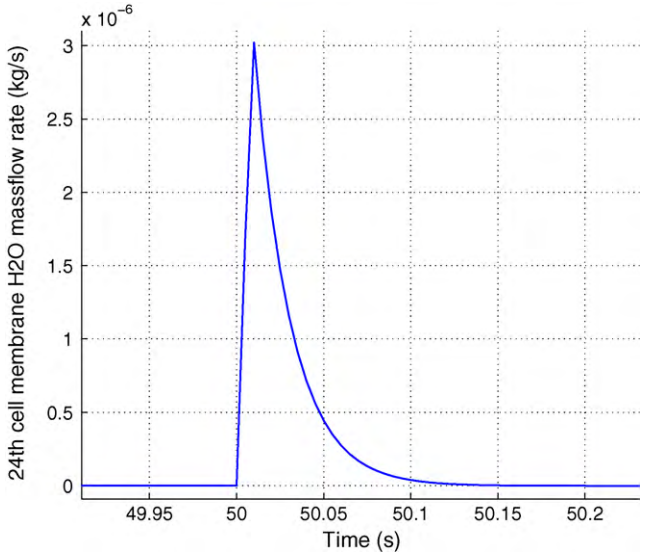

Fig. 29. 2nd test: membrane water mass flow dynamic response at 50 s.

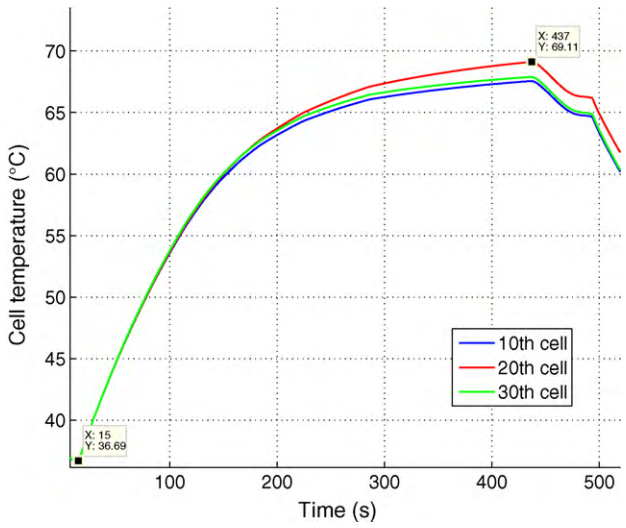

Fig. 30. Cells temperature dynamic response at step current 44 A.

with:

$$k_{\text{mem}} = \frac{\delta_{\text{mem}}}{(0.5193\,\lambda - 0.326)S} \tag{53}$$

$$k_{\text{sources}} = -\frac{i\,\Delta S}{2F} - 0.011\, i^2\, k_{\text{mem}} \tag{54}$$

In steady-state, the left hand side of (51) becomes zero. Using (29) and (30), the expression of cell temperature T_{cell} in steady-state can be calculated:

$$T_{\text{cell\_Final}} = \frac{(i\,\eta_{\text{act}} + 4.2\, i^2\, k_{\text{mem}} + h_{\text{forced}} S_{\text{contact}} T_{\text{coolant}} + h_{\text{nat\_radia}} S_{\text{ext}} T_{\text{amb}})}{h_{\text{forced}} S_{\text{contact}} + h_{\text{nat\_radia}} S_{ext} - k_{\text{sources}}} \tag{55}$$

Thus, the temperature dynamic in transient state can be obtained in a general first order dynamic form:

$$\frac{\rho_{\text{cell}}\, V_{\text{cell}}\, C_p}{h_{\text{forced}}\, S_{\text{contact}} + h_{\text{nat\_radia}} S_{\text{ext}} - k_{\text{sources}}} \cdot \frac{\mathrm{d}T_{\text{cell}}}{\mathrm{d}t} + T_{\text{cell}} = T_{\text{cell\_Final}} \tag{56}$$

Replacing k_{sources} by its expression the cell level temperature time constant in thermal domain can be obtained:

$$\tau_{\text{thermal}} = \frac{\rho_{\text{cell}}\, V_{\text{cell}}\, C_p}{\left(h_{\text{forced}} S_{\text{contact}} + h_{\text{nat\_radia}}\, S_{\text{ext}} + \frac{i\,\Delta S}{2F} + \frac{0.011\,\delta_{\text{mem}} i^2}{(0.5193\,\lambda - 0.326)S}\right)} \tag{57}$$

With the Ballard 1.2 kW fuel cell stack, using the fuel cell stack properties data in [20], the fuel cell temperature transient time constant in the thermal domain can be estimated between 37.15 s and 124.3 s. Thus the cell temperature transient state can last about 497 s (8 min 17 s).

The figures below present the 10th, 20th and 30th cell temperature results with the stack current profile shown in Fig. 3. According to Eqs. (31)–(33), when the stack current changes, the generated heat in the fuel cell changes. The cell temperature varies during a transient period in order to achieve to the new equilibrium point. From the figures results, it can be concluded that the stack temperature transient time for a current step change should be larger than 422 s as in Fig. 30 and larger than 221 s as in Fig. 31.

4. Fuel cell stack spatial non-homogeneity

Another important point in a fuel cell stack system is the spatial non-homogeneity between the cells.

In a fuel cell stack, all cells have the same properties, such as geometry and material. But during the stack operation, each cell has

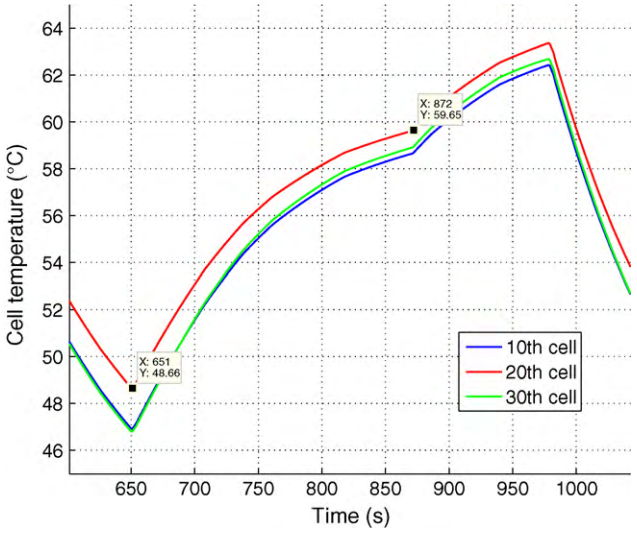

Fig. 31. Cells temperature dynamic response at step current 35 A.

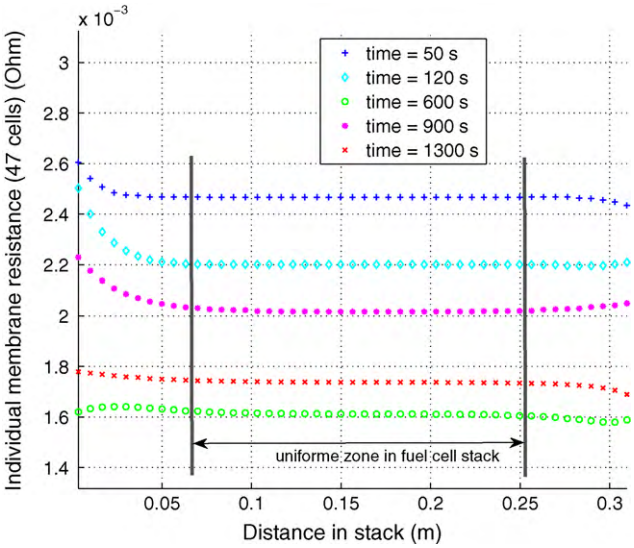

Fig. 33. Membrane resistances in stack at different times.

its own state conditions, such as voltage, channels pressures, temperature, depending on the boundary conditions from the adjacent cells.

Thus, the non-homogeneous effect through the fuel cell stack can be observed experimentally as shown in Fig. 6 and Figs. 10–12.

4.1. Spatial non-homogeneity analysis in different physical domains

From the proposed model and stack current profiles presented in Fig. 3, the non-homogeneity can be observed in each physical domain from the Ballard 1.2 kW fuel cell stack simulation results.

In electrical domain, the cell voltages and membrane resistances non-homogeneity are illustrated in Figs. 32 and 33. The cells at the beginning and at the end of the stack form a significant non-homogeneous zone at different times, but the cells in the middle of the stack are almost homogeneous. The homogeneous zone can be observed from the 11th cell to the 38th cell in the stack (47 cells overall).

The similar non-homogeneity can be also observed in the fluidic domain. The oxygen partial pressures in each cell cathode channels and the hydrogen partial pressures in the anode channels are given for different times in Figs. 34 and 35. In addition, the spatial distribution of individual membrane water contents is presented in Fig. 36. From the figures, the fluidic domain homogeneous zone can be decided from the 10th cell to the 37th cell.

In the thermal domain, due to the stack low boundary temperature conditions, the cells at the end of the stack have a lower temperature compared to the middle ones. Depending on the cell operating temperature (higher temperature with a higher power output), the temperature homogeneous zone can be very different, as shown in Fig. 37. It has to be noted that the temperature profile shown in Fig. 37 is the detailed cell layer level temperatures (remember that 1 cell has 10 single layers).

Since the electrochemical reaction takes place in the cathode catalyst layer, this layer has the highest temperature in the cell, which is shown by the temperature spike in each cell positions. From the results, the temperature homogeneous zone can be defined from the 14th cell to the 38th cell in the stack (at $t = 900$ s). However, in a general consideration, this homogeneous zone can

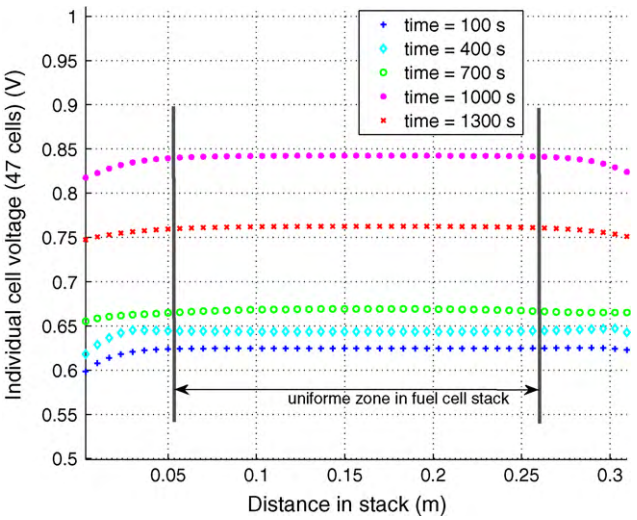

Fig. 32. Cell voltages in stack at different times.

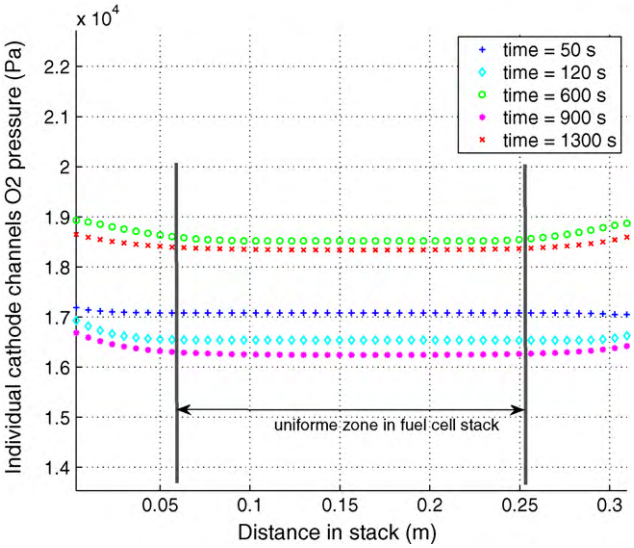

Fig. 34. Oxygen pressures in the channels at different times.

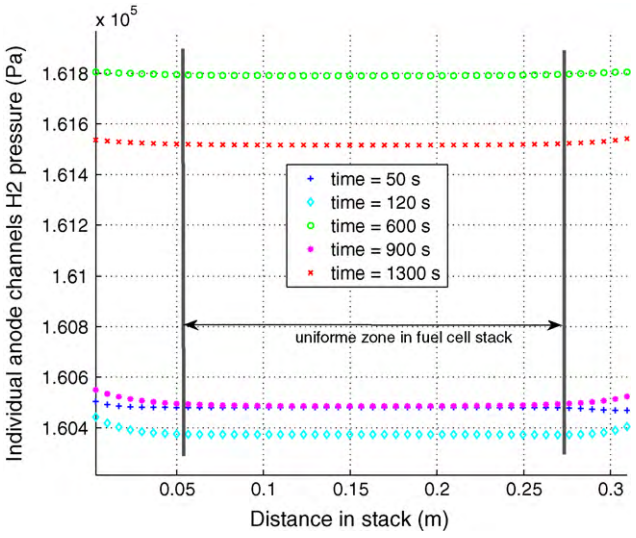

Fig. 35. Hydrogen pressures in the channels at different times.

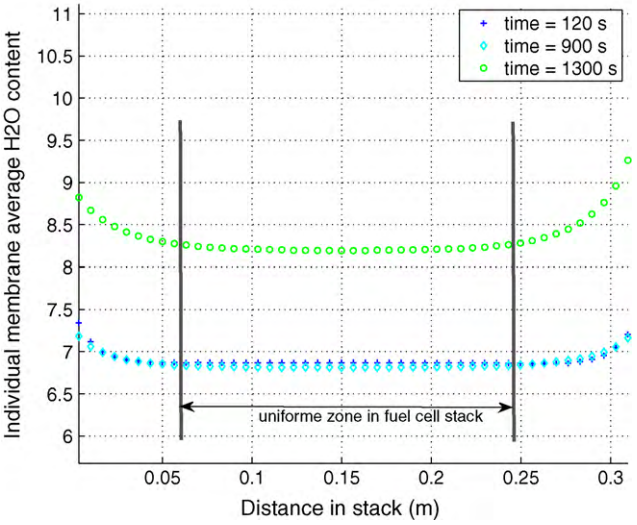

Fig. 36. Membrane water contents at different times.

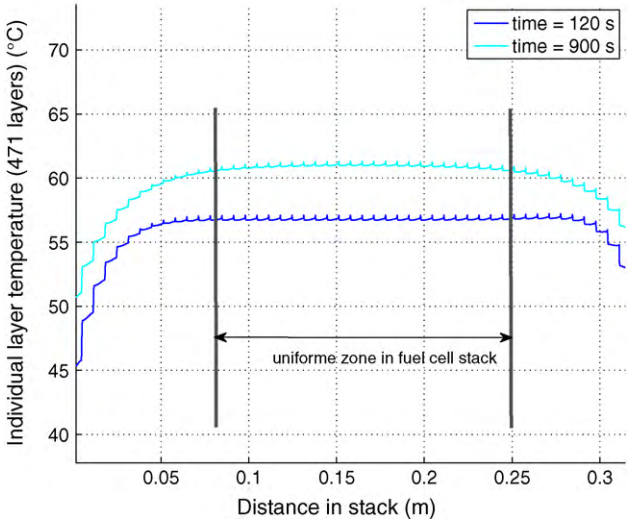

Fig. 37. Detailed cell layers temperatures in stack at different times.

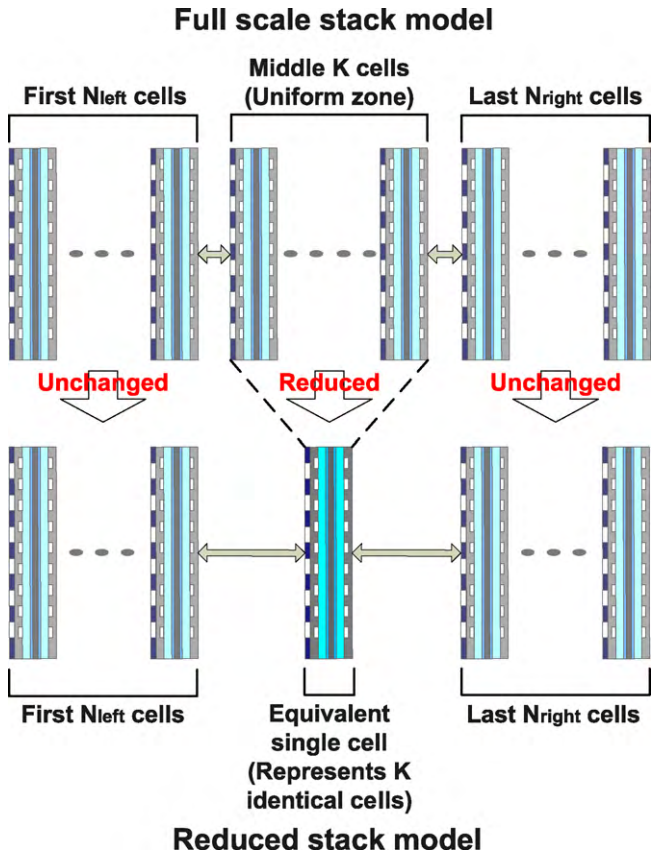

Fig. 38. Stack model reduction method.

be reasonable approximated from the 8th cell to the 43rd cell as for time at 120 s.

5. Stack model spatial reduction method

5.1. Modelling considerations and stack model redecution method

On the one hand, from the analyses in the previous section, it can be concluded that the cells at the end of fuel cell stack have an important non-homogeneity in all physical domains. On the

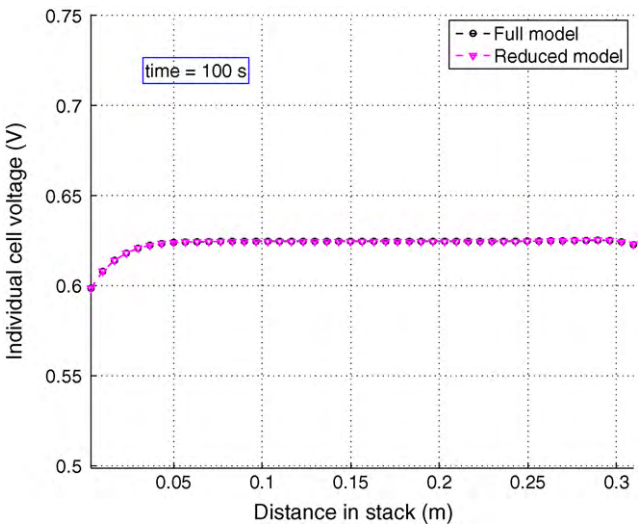

Fig. 39. Cell voltages spatial comparison at 100 s.

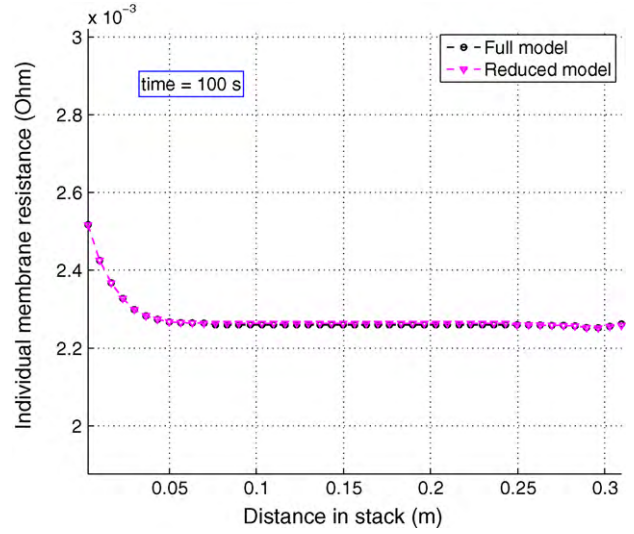

Fig. 40. Cell membrane resistances spatial comparison at 100 s.

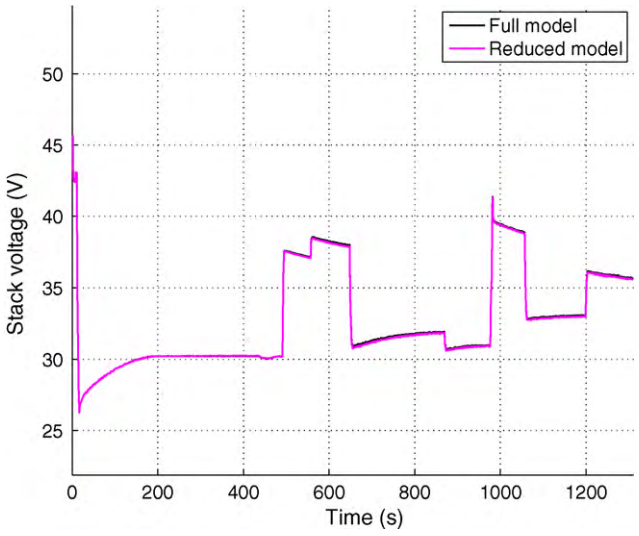

Fig. 41. Stack voltage temporal comparison.

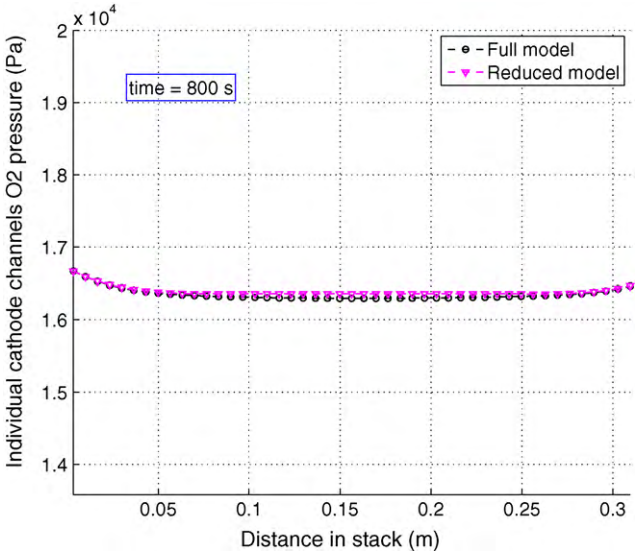

Fig. 42. Oxygen pressures in channels spatial comparison at 800 s.

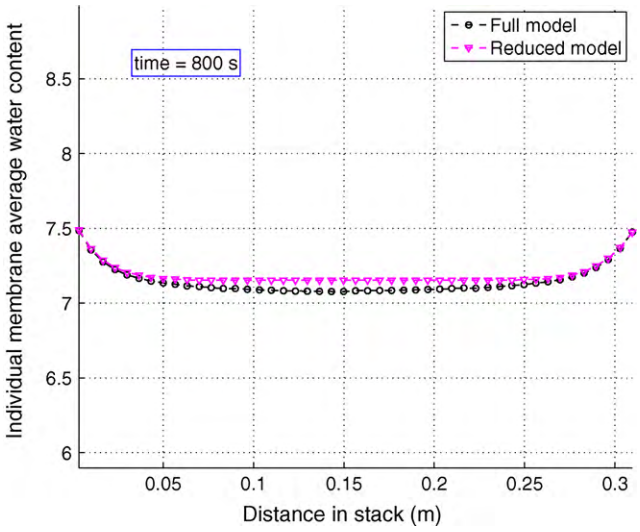

Fig. 43. Membrane water contents spatial comparison at 800 s.

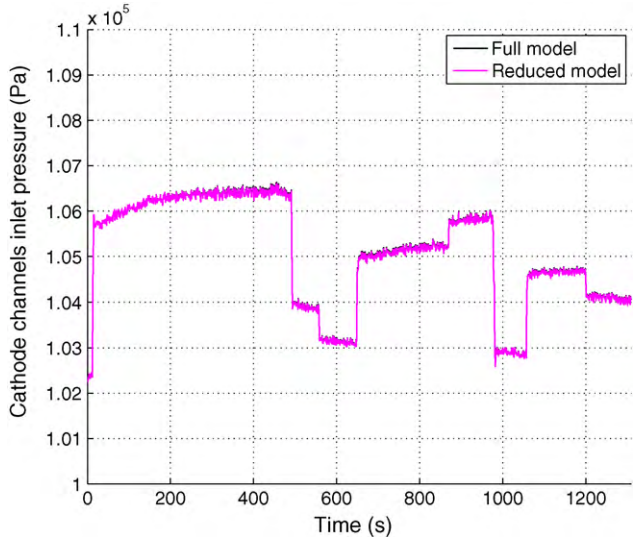

Fig. 44. Cathode inlet pressure temporal comparison.

other hand, most cells in the middle of the stack (homogeneous zone) have almost the same physical states in electrical, fluidic and thermal domains.

Thus, for modelling reduction purposes, since the cells in the middle of the stack have the same behaviour during the simulation, the *k*-cells in the homogeneous zone of the stack can be reduced to a single equivalent cell in the model, and the cells at end of the stack will be kept as full scale model, in order to predict accurately the non-homogeneity effects in the stack, as shown in Fig. 38. The results of this equivalent cell will be duplicated *k* times to give the *k* cells outputs in the middle of the stack.

Since the homogeneous zone is quite large in a fuel cell stack, with this reduction method, the simulation time can be significantly reduced, and the accuracy of the model is still kept.

It has to be noted that, the determination of the homogeneous zone in the fuel cell stack can only be achieved empirically from the full scale stack model simulation results. The full scale model should be simulated at least once before to determine this zone.

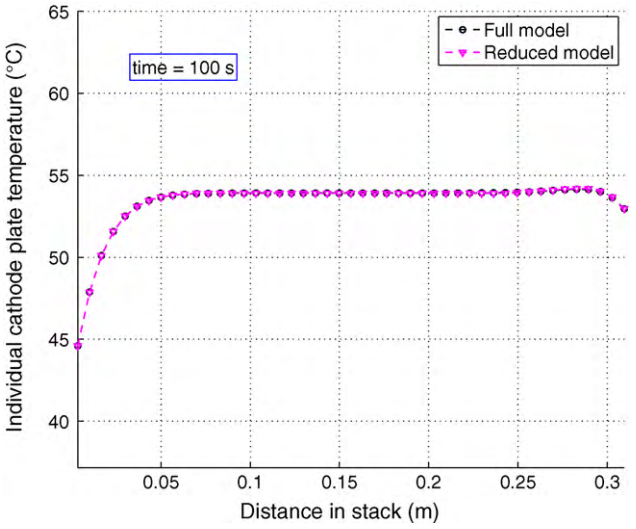

Fig. 45. Cathode bipolar plates temperatures spatial comparison at 100 s.

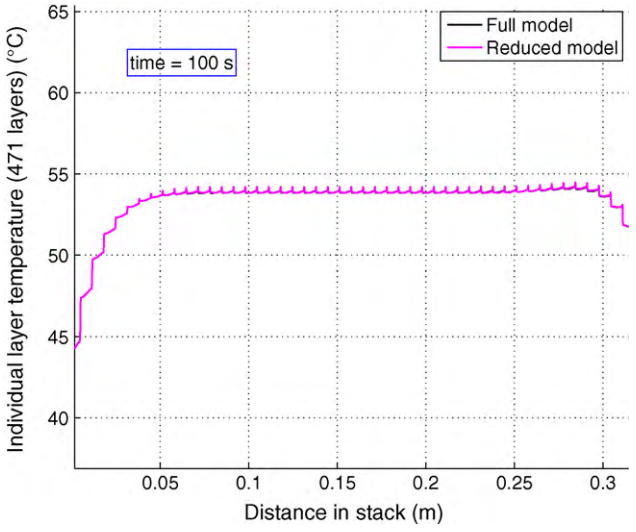

Fig. 46. Cell layers temperatures spatial comparison at 100 s.

5.2. Comparison between the reduced stack model and full model

In the Ballard 1.2 kW fuel cell stack simulations, from the results in the previous sections, the non-homogeneous zone of the stack model is decided to be the first 10 cells and the last 10 cells in the stack. The 27 cells in the middle of the stack are considered to have a homogeneous behaviour in different physical domains.

Thus, the 47 cells stack model is reduced to a 21 cells stack model during the simulation, with 1 equivalent cell that represent 27 cells in the middle of the stack. The simulation value results of this equivalent cell are duplicated 27 times in order to have the overall 47 cells results.

In order to validate the proposed model reduction method, a full scale stack model simulation and a reduced stack model simulation have been carried out with the same stack boundary conditions. The comparison between the two models in different physical domains is shown hereafter.

In the electrical domain, the model spatial comparison for the cell voltages and membrane resistances are given in Figs. 39 and 40. It can be seen that the cells in the homogeneous zone have almost the same physical value.

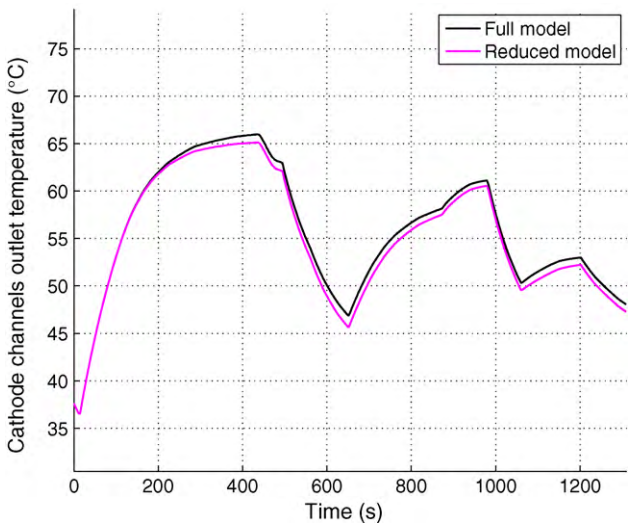

Fig. 47. Cathode air outlet temperature temporal comparison.

The temporal comparison for the entire stack voltage is shown in Fig. 41. The stack voltage of the reduced model is almost as the same as the full scale model over 1 300 s.

In the fluidic domain, the spatial comparison is shown for $t =$ 800 s. The individual cathode channel oxygen partial pressure are given in Fig. 42. The membrane water content is illustrated in Fig. 43. The results demonstrate a good agreement between the reduced model and the full scale model. The slight error between the results can be seen in the figures. This error is due to the homogeneous zone definition. In fact, for some physical state variables, such as membrane water content, the choice for the first 10 cells and the last 10 cells as non-homogeneous zone is not always perfectly correct. On the one hand, from the full scale model, it can be noted that the non-homogeneous zone is larger than 20 cells. But on the other hand, the relative error in the figures is less than 2% with the chosen homogeneous zone. The slight relative error can be balanced by the gained time during the simulation with less non-homogeneous cells. Thus, the results are acceptable.

A temporal validation for the cathode channels inlet pressure is also given in Fig. 44. The results from the two models show a very good agreement.

In the thermal domain, the reduced model is validated spatially for individual cathode bipolar plate temperature and individual cell layer temperature, as shown in Figs. 45 and 46. Again, it can be concluded that the proposed reduced model has a very good accuracy in the thermal domain compared to the full scale stack model. The stack cathode air outlet temperature temporal prediction is shown in Fig. 47. The maximum error of the reduced model is less than 0.5% over 1 300 s.

5.3. Reduced stack model advantages

The proposed model reduction method has two major advantages for the fuel cell model development.

Firstly, the proposed method can accelerate significantly the simulation speed keeping at the same time the model non-homogeneity and the model accuracy as in the full scale model. With the appropriate homogeneous zone choice between the model simplicity and model accuracy, the reduced multi-physical stack model can be simulated in real time. In the case of the Ballard 1.2 kW fuel cell stack model, the reduced model can be run 6 times faster than the full scale model.

Secondly, the reduced model has much less simultaneous differential equations compared to the full model. Thus,

the numerical stability of the mathematical solver can be improved.

6. Conclusion

In this paper, a one-dimensional, multi-physical, dynamic fuel cell stack model has been presented. The proposed model covers 3 major physical domains: electrical, fluidic and thermal. In each domain, the corresponding dynamic physical model has been introduced. The stack model is obtained by combining the individual cell models. The stack model is validated temporally and spatially against a Ballard Nexa 1.2 kW 47 cells fuel cell stack. The simulation results demonstrate a very good accuracy with the experimental results in different physical domains.

In the second part, a detailed fuel cell dynamic time constants analysis in electrical, fluidic and thermal domains has been preformed. The time constant formulation in each domain has been given explicitly. For the Ballard Nexa fuel cell stack, the voltage electrical dynamic time constant is about 0.16 s. In the fluidic domain, the cooling channels pressure time constant is about 8.14 μs, the one of the cathode channels is about 6.92 ms and about 25.1 ms for anode channels. On the other hand, the membrane water diffusion time constant can be estimated between 0.0082 s and 0.12 s depending on the membrane water contents. The most significant time constant has been found to be in the thermal domain. For the Ballard fuel cell stack, the cell temperature dynamic time constant is estimated to be between 37.15 s and 124.3 s. These values can give a general idea of the fuel cell dynamic transient time consideration.

Beside the dynamic analysis, the non-homogeneity across the fuel cell stack has also been discussed. From the model results, a novel stack model spatial reduction method has been proposed in order to reduce the simulation time. The spatial reduced models results have been compared to the full model results. The comparison demonstrates that the reduced model can predict the entire stack behaviour with a great accuracy, but with much less simulation time. This kind of reduction method can be applied in order to achieve real time simulations, for example in Hardware-in-the-Loop applications.

References

[1] U. Krewer, K. Sundmacher, Journal of Power Sources 154 (1) (2006) 153–170.
[2] W.-M. Yan, C.-Y. Soong, F. Chen, H.-S. Chu, Journal of Power Sources 143 (1–2) (2005) 48–56.
[3] Q. Yan, H. Toghiani, H. Causey, Journal of Power Sources 161 (1) (2006) 492–502.
[4] M.U. Iftikhar, D. Riu, F. Druart, S. Rosini, Y. Bultel, N. Retiére, Journal of Power Sources 160 (2) (2006) 1170–1182.
[5] Z. Lemes, A. Vath, T. Hartkopf, H. Mäncher, Journal of Power Sources 154 (2) (2006) 386–393.
[6] J. Zou, X.-F. Peng, W.-M. Yan, Journal of Power Sources 159 (1) (2006) 514–523.
[7] H. Wu, X. Li, P. Berg, International Journal of Hydrogen Energy 32 (12) (2007) 2022–2031.
[8] R.N. Methekar, V. Prasad, R.D. Gudi, Journal of Power Sources 165 (1) (2007) 152–170.
[9] H. Meng, Journal of Power Sources 171 (2) (2007) 738–746.
[10] T. Yalcinoz, M.S. Alam, Journal of Power Sources 182 (1) (2008) 168–174.
[11] H. Sun, G. Zhang, L. Guo, H. Liu, International Journal of Hydrogen Energy 34 (13) (2009) 5529–5536.
[12] Y. Lee, B. Kim, Y. Kim, International Journal of Hydrogen Energy 34 (4) (2009) 1999–2007.
[13] B. Blunier, A. Miraoui, Pile à combustible (French), Ellipses, Paris, 2007.
[14] H. Ju, H. Meng, C.-Y. Wang, International Journal of Heat and Mass Transfer 48 (7) (2005) 1303–1315.
[15] J. Park, X. Li, Journal of Power Sources 162 (1) (2006) 444–459.
[16] S. Maharudrayya, S. Jayanti, A.P. Deshpande, Journal of Power Sources 157 (1) (2006) 358–367.
[17] M. Khandelwal, S. Lee, M.M. Mench, Journal of Power Sources 172 (2) (2007) 816–830.
[18] S.-K. Park, S.-Y. Choe, Journal of Power Sources 179 (2) (2008) 660–672.
[19] F. Gao, B. Blunier, A. Miraoui, A.E. Moudni, IEEE Transactions on Industrial Electronics 57 (6) (2010) 1853–1864.
[20] F. Gao, B. Blunier, A. Miraoui, A.E. Moudni, International Journal of Hydrogen Energy 34 (13) (2009) 24.
[21] J. Larminie, A. Dicks, Fuel Cell Systems Explained, 2nd edition, Wiley, 2003.
[22] R. O'Hayre, S.-W. Cha, W. Colella, F.B. Prinz, Fuel Cell Fundamentals, 1st edition, John Wiley & Sons, Inc., 2005.
[23] J.M. Corrêa, F.A. Farret, L.N. Canha, M.G. Simões, IEEE Transactions on Industrial Electronics 51 (5) (2004) 10.
[24] T. Springer, T. Zawodzinski, S. Gottesfeld, Journal of Electrochemical Society 138 (8) (1991) 9.
[25] F. White, Fluid Mechanics, 4th edition, McGraw Hill, 1998, pp 340.
[26] D.M. Bernardi, M.W. Verbrugge, AIChE Journal 37 (8) (1991) 13.
[27] Incropera, DeWitt, Bergman, Lavine, Fundamentals of Heat and Mass Transfer, 6th edition, vol. 1, Wiley, 2007.